Jan *et al. Terrestrial, Atmospheric and Oceanic Sciences* (2025) 36:29
https://doi.org/10.1007/s44195-025-00113-w

Terrestrial, Atmospheric and Oceanic Sciences

RESEARCH Open Access

Turbulence and eddy regional exchange in the western North Pacific: joint oceanic and atmospheric experiment using R/V New Ocean Researcher 1

Sen Jan[1*], Yiing Jang Yang[1], Ming-Huei Chang[1], Je-Yuan Hsu[1], Kai-Chieh Yang[1], Emmy Tsuiyu Chang[1], Shih-Hong Wang[1], Yu-Hsin Cheng[2], Jia-Lin Chen[3], Ying-Chih Fang[4], Wei-Yu Chang[5], Chung-Hsiung Sui[6], Ming-Jen Yang[6], Po-Hsiung Lin[6], An-Yi Tsai[7] and Chung-Chi Chen[8]

Abstract

Sponsored by the National Science and Technology Council of Taiwan, the programs Sailing to the Blue Sea (SBS), Kuroshio to Turbulence Exchange (KTEX), and the U.S.-Taiwan collaboration program Island Arc Turbulent Eddy Regional Exchange (ARCTERX) jointly conducted a multidisciplinary field campaign aboard the R/V New Ocean Researcher 1 from March 25 to April 19, 2024. The cruise completed a round trip from Kaohsiung to Palau, executing coordinated oceanic and atmospheric observations in the western North Pacific. The scientific objectives of this campaign were to: (1) investigate the physical, biological, and biogeochemical properties of a targeted cyclonic mesoscale eddy in the western North Pacific and its impact on oceanic weather through air-sea interactions; (2) quantify water mass transformation and nutrient flux variability from the North Equatorial Current (NEC) to the Kuroshio; (3) examine the diurnal warm layer and its coupling with atmospheric boundary layer variability in the subtropical and tropical regions; (4) detect potential ground motion in the Philippine Sea basin at the eastern flank of the Gagua Ridge, east to Taiwan; and (5) measure along-track gravity anomaly across the Philippine Sea basin. The campaign successfully sampled a cyclonic eddy centered at (131°E, 18°N), hydrographic transects across the Kuroshio and the NEC, and high-resolution upper ocean temperature profiles in the tropical ocean. To facilitate detailed analyses of the complex cruise data, the ship-based and autonomous observations are introduced here.

Highlights

- Physical and biological properties of a cyclonic mesoscale eddy are observed.
- Atmospheric conditions are measured along the cruise track and over the eddy.
- Ground motion and along-track gravity anomaly in the Philippine Sea basin are measured.

Keywords Eddy, Turbulence, Air-sea interaction, Kuroshio, Western North Pacific, Biology

*Correspondence:
Sen Jan
senjan@ntu.edu.tw

Full list of author information is available at the end of the article

1 Introduction

Field observations, high-resolution satellite imagery, and numerical simulations have shown that mesoscale eddies (with diameter ~ 100–300 km), submesoscale processes (with length scales ~ 10–100 km), and turbulence are ubiquitous features in the ocean circulations (e.g., Molemaker et al. 2015; McWilliams 2016). These multiscale processes significantly influence energy exchange, water mass distribution, and current variability in the Kuroshio region. They also shape broader patterns of ocean circulation, influence both vertical and horizontal biological processes, and affect the distribution of biogeochemical properties, with consequences that extend to the global climate system. This dynamic complexity is illustrated in Fig. 1. From a dynamical perspective, the energy cascade process—from large-scale motions to progressively smaller scales where energy is ultimately dissipated—is fundamental to understand the distribution and balance of the approximately 1 Terawatt (1 Terawatt = 10^{12} Watts) of energy imparted to the ocean by atmospheric winds (Wunsch 1998; Alford 2003; Thomas et al. 2008). Understanding these processes and their interactions, particularly those involving air–sea exchanges, is therefore essential for advancing our knowledge of global climate dynamics. However, comprehensive field experiments, particularly in the western North Pacific, remain limited, constraining our ability to fully resolve their roles and interactions (Centurioni et al. 2022; Tech. Rep.).

It is known that the western North Pacific is strongly influenced by mesoscale eddies, which regulate momentum, heat, and salt fluxes and mediate ocean–atmosphere interactions (Chelton et al. 2007; Cheng et al. 2014; Ueno et al., 2023, among others). These eddies also affect nutrient supply, primary productivity, and ecosystem structure (McGillicuddy 2016 and 2017; Ueno et al., 2023). Regional circulation, together with eddy activity, influences Pacific-wide dynamics and water mass variability (e.g., Rudnick et al. 2015). Between ~ 10°–15° N, the westward-flowing North Equatorial Current (NEC) bifurcates near the Philippines into the northward Kuroshio and southward Mindanao Current, while farther north the Subtropical Countercurrent (STCC) contributes to eddy generation and regional climate variability (e.g., Kang et al. 2010; Kobashi and Kubokawa 2012; Qiu

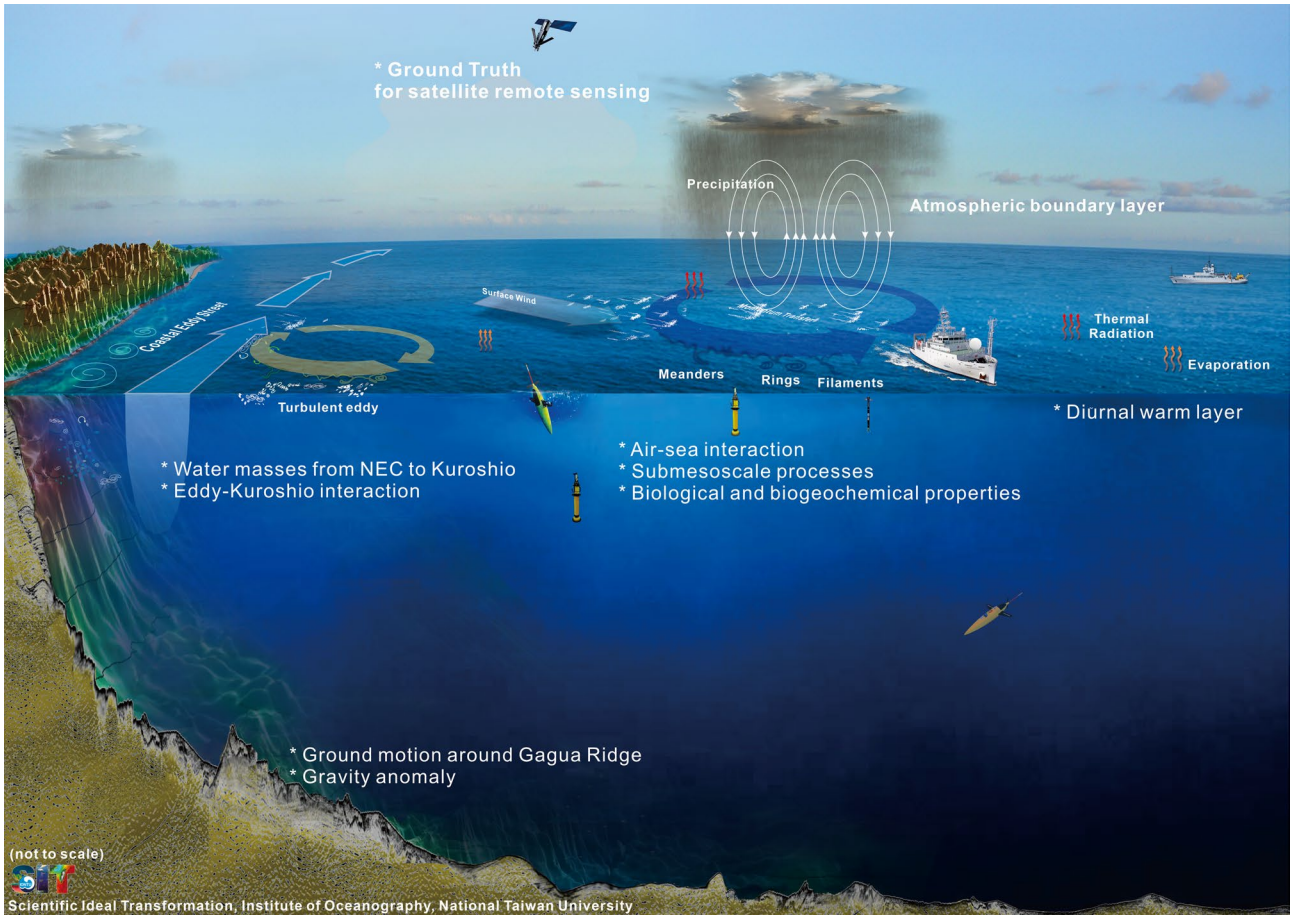

Fig. 1 Conceptual diagram illustrating complex physical processes in the upper ocean and their interactions with the atmosphere in the western North Pacific

et al. 2014). Despite the aforementioned investigation on energy cascade and air-sea interactions, the processes by which mesoscale eddies interact with boundary currents and influence water mass properties in this transition zone remain insufficiently quantified. Furthermore, in situ observations that capture the coupled physical–biogeochemical influences of these eddies in the study region are still meager, leaving important gaps in our understanding of their role in regional and basin-scale variability.

To gain a detailed understanding of these multiscale ocean processes, the Sailing to the Blue Sea (SBS) and Kuroshio and Turbulence Exchange (KTEX) programs, sponsored by Taiwan's National Science and Technology Council (NSTC), partnered with the Island Arc Turbulent Eddy Regional Exchange (ARCTERX) project, funded by the U.S. Office of Naval Research (ONR), to initiate a series of joint field experiments beginning in 2022. This international collaboration addresses the critical need to evaluate the larger-scale impacts of submesoscale dynamics on ocean circulation and predictability. However, this effort faces significant technological challenges due to the vast spatial and temporal variability involved. Traditional ship-based measurements alone are inadequate to resolve the fine-scale features and continuous variability of submesoscale processes. Instead, the study employs a network of autonomous platforms capable of sustained, high-density observations over expansive areas and extended durations to capture submesoscale flows effectively. By integrating multi-platform measurements, the joint campaign aims to characterize submesoscale dynamics in the Kuroshio region and across the broader western Pacific Ocean, spanning the area between the Luzon and Mariana Island arcs (Centurioni et al. 2022; Tech. Rep.).

In addition to their physical importance, mesoscale eddies play a crucial role in shaping biological and biogeochemical properties in the ocean. In marine ecosystems, picoplankton populations are microbial components of plankton communities that include picophytoplankton and heterotrophic bacteria (HB). They are also crucial to the biogeochemistry and dynamics of the marine food web (Azam and Malfatti 2007). Picophytoplankton communities, *Synechococcus* (SYNE), *Prochlorococcus*, (PRO) and *Picoeukaryotes* (PE) contribute substantially to the total phytoplankton biomass in marine ecosystems, usually contributing 50–90% of the total chlorophyll *a* in oligotrophic waters (Agawin et al. 2000). A lot of attention has recently been paid to the impact of mesoscale eddies on phytoplankton communities (McGillicuddy et al. 2007; McGillicuddy 2016). It has been shown that cold eddies during the developmental phase frequently showed higher Chl a, a higher proportion of PRO, and a decrease in SYNE (McGillicuddy et al. 2007) as a result of eddy-driven upwelling, which may provide significant amounts of nutrients to support primary productivity in the subtropical oceans. Additionally, picophytoplankton maintained its dominance regardless of cold or warm eddies in tropical and subtropical open waters, where PRO was responsible for up to 82% of phytoplankton primary productivity (Casey et al. 2007).

In addition to picoplankton, HB is a major consumer of dissolved organic matter (DOM) and plays a significant role in nutrient and carbon cycling (Ducklow 1999). Though the primary productivity and chlorophyll within these mesoscale features are relatively high, little information is available regarding how HB responds to mesoscale eddies. The HB response caused by eddy-induced upwelling is complex and not fully understood. In some studies, bacterial abundance is higher in cold-core eddies of the NE Atlantic (Thyssen et al. 2005), while others have found no difference between bacterial biomass inside and outside cyclonic eddies (González-Benítez et al. 2001; Tarran et al. 2001). Additionally, there are limited studies on associated bacterial production (BP) response to eddy-induced phytoplankton blooms, where in one study by Bode et al. (2001) found higher BP near the Canary Islands in a cold-core eddy area than in surrounding waters. In general, viruses (VIR) affect the ecology and biogeochemistry of oceans as well as microbial mortality (Suttle 2005). However, the causes of VIR distribution and extent in cyclonic eddies and the relationship between bacteria and viruses are still poorly understood. It is particularly noteworthy that little is known about VIR abundance and spatial variation responses associated with cold eddies from the surface to deeper waters (such as 1000 m).

Understanding these processes in the context of physical dynamics and air-sea exchanges over eddies, was a key objective proposed by KTEX. Submesoscale features, including fronts, eddies, filaments, and instabilities associated with mesoscale eddies, serve as critical intermediaries between mesoscale processes and small-scale turbulence. These features can strongly modulate biological and biogeochemical parameters associated with mesoscale eddies. Accordingly, the biological sampling of this observation focuses on characterizing environmental variability across a cold-core cyclonic eddy and examining its influence on microbial community structure. In particular, vertical distribution patterns of autotrophic picoplankton (PRO, SYNE, and PE) and HB, as well as viruses from the surface to deeper waters (1000 m depth) across a cold eddy are examined. This study hypothesizes that the upward advection of deep and relatively cold nutrient-rich water within cyclonic cold eddies increases PE abundance and HB abundance. This project aims to provide a comprehensive view of biological responses to mesoscale eddies, emphasizing the importance of

integrating biological, physical, and chemical factors into explaining how mesoscale eddies affect oceanic biogeochemistry through the in-situ observations.

Furthermore, mesoscale eddies, whether cold-core (upwelling) or warm-core (downwelling), are thought to impact the lower atmospheric boundary layer (ABL) by modulating surface fluxes and atmospheric stability. The diurnal warm layer (DWL), which develops during daytime under calm winds and solar radiation, can alter latent and sensible heat fluxes, thereby influencing the transfer of heat and moisture to the atmosphere and subsequently increases convective instability in the ABL (e.g. Shevchenko et al. 2023). Its effects are particularly pronounced in subtropical and tropical oceans, where solar heating and calm conditions are frequent. Using high spatiotemporal resolution observations, the scientific objective is to investigate the kinematic/microphysical structure and time-space characteristics of the marine ABL over mesoscale eddies. To address the mechanisms and extent of these eddy-atmosphere interactions and achieve the collaborative goals of the SBS, KTEX, and ARCTERX programs, an interdisciplinary field campaign was conducted aboard Taiwan's R/V New Ocean Researcher 1 (hereafter NOR1) in late spring 2024.

Apart from the eddy-related study, a marine geophysical survey was conducted in conjunction with the cruise, making use of shared ship time and logistics. A seafloor tiltmeter mooring was deployed on the eastern flank of the Gagua Ridge in late 2023, continuously recording ground tilt. During the cruise, this mooring was successfully recovered. By detecting subtle shifts frequently undetectable with conventional seismic instruments, tiltmeters enhance our ability to monitor seafloor stability and to understand the coupling between solid Earth deformation and oceanographic forcing. In this report, we present the tilt time series, which, for the first time, show the potential ground motion and the influence of ambient water perturbation. In addition, shipborne gravity data were collected during the cruise, enabling studies of seafloor morphology, crustal structure, and tectonic processes. The campaign featured integrated multiparameter measurements, enabling a comprehensive assessment of coupled processes across the ocean-atmosphere interface in the presence of mesoscale eddies and demonstrating the potential of cross-disciplinary cooperation and operation. The primary objectives of this cruise were to:

1) investigate the physical, biological, and biogeochemical characteristics of a targeted cyclonic mesoscale eddy in the western North Pacific, and evaluate its influence on oceanic weather via air-sea interactions;
2) quantify the variability of water mass and nutrient fluxes from the NEC to the Kuroshio;
3) examine the formation and variability of the diurnal warm layer and its impact on the ABL in subtropical and tropical seas;
4) detect potential ground motion in the western Philippine Sea basin near the Gagua Ridge east of Taiwan detected by seafloor tiltmeters (hereafter referred to as CTTL);
5) conduct the gravity measurement across the Philippine sea basin.

Tasks 4) and 5) were undertaken through collaborative efforts in marine geophysics and geodesy, in alignment with the NSTC's policy to optimize individual cruises by supporting multiple scientific objectives.

This article presents a synthesis of data collected during the field observations and highlights the preliminary results, offering insights into the multifaceted roles of mesoscale eddies and pioneering experiments in sea-basin exploration.

2 Observations

This NOR1 cruise was split to two legs: NOR1-0069 A from 25 March to 5 April and NOR1-0069B from 8 April to 19 April, 2024. The atmospheric condition in the spring 2024 was in the decaying phase of the 2024 ENSO event. The northwest Pacific was influenced by an anomalously strong descending air and low-level anticyclonic (divergent) circulation in the lower troposphere (Fig. 2). The above atmospheric circulation is forced by tropical warm sea surface temperature (SST) anomalies (Wang et al. 2000; Lee et al. 2023 and references therein). During the NOR1-0069 cruise, a cyclonic eddy (2024CE) was selected and observed (Fig. 3), with observations and sampling coordinates summarized in Tables 1 and 2, respectively. Unfortunately, the shipboard 75- and 150-kHz acoustic Doppler current profiles malfunctioned throughout the entire cruise.

The satellite sea level anomaly (SLA) obtained from the Copernicus Marine Service (available at https://doi.org/10.48670/moi-00148) indicates the center of the we stward-propagating cyclonic eddy was located at (131°E, 18°N), with a diameter of ~220 km on 27 March 2024 (Fig. 3). Measurements collected through 2024CE (stations A0-A6 in Fig. 3; Table 1) include conductivity-temperature-depth (CTD) profiles, vertical distribution of biological parameters from seawater samples, and turbulence kinetic energy (TKE) dissipation rates (ε) observed by a microstructure profiler (VMP-250). Additionally, the cruise deployed two EM-APEX autonomous profiling floats at both the edge and the center of the 2024CE, as well as a Seaglider southeast of the eddy. The Seaglider transected the 2024CE from southeast to northwest,

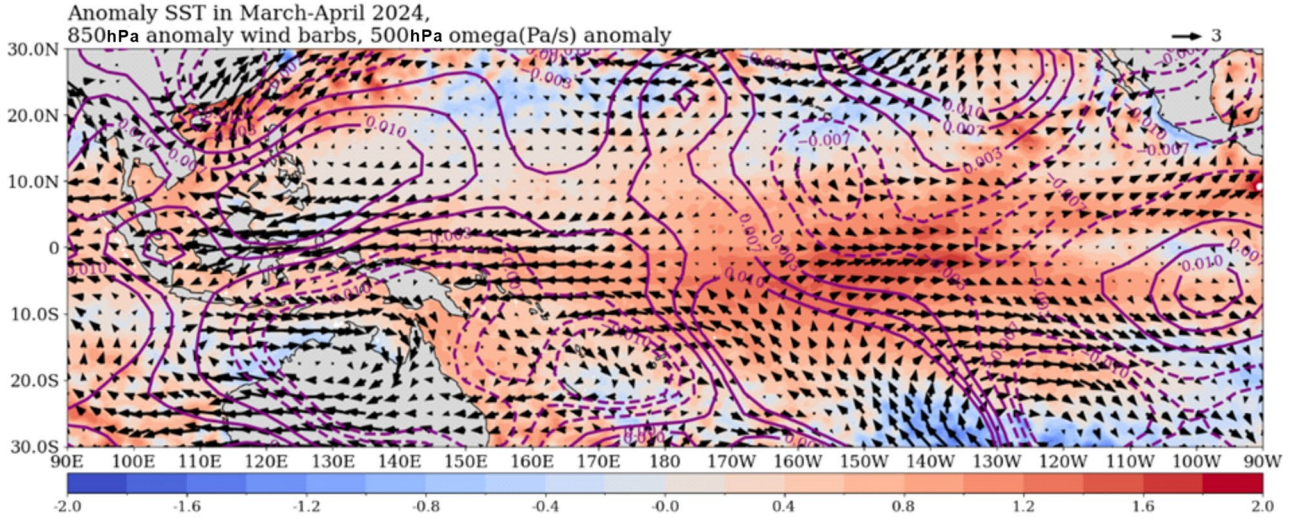

Fig. 2 Time mean anomalies of SST (shadings in °C), 850-hPa wind (vectors in m s^{-1}) and 500-hPa p-velocity (contours) for the period of March and April 2024

providing high-resolution hydrographic data, including temperature, salinity, dissolved oxygen, fluorescence, and optical backscatter.

Apart from observations of the 2024CE, the NOR1-0069 cruise also performed CTD measurements along its track across the Kuroshio (stations K1-K3) and the North Equatorial Current (stations N1-N6). Finally, a Ship-based Air-sea Flux and Exchange System (SAFE) T-bar air-sea meteorological drifting platform was deployed in the tropical region between 9°N and 10°N to observe diurnal warm layer processes from 2 to 10 April 2024. The radiosondes were launched every three hours in the eddy region, while in other areas, they were launched every 12 h (at 8 am and 8 pm local time).

2.1 Seaglider and EM-APEX floats observations

The Seaglider (serial no. SG628) used in this study was equipped with unpumped Sea-Bird conductivity and temperature sensors (CT Sail). The resolution of the sensor is 0.0001 °C for temperature and 0.001 for salinity, with sampling rates of 5 s (approximately every 0.75 m) above 250 m and 10 s (approximately every 1.5 m) below 250 m. Given an averaged glider vertical speed of 0.15 m s^{-1} and a vertical to horizontal ratio of approximately 1:3, the horizontal resolution ranged from 2.25 to 4 m between consecutive water column samples. The initial data process follows the Seaglider Quality Control Manual (available at https://gliderfs2.coas.oregonstate.edu/sgliderweb/Seaglider_Quality_Control_Manual.html), which allows the accuracies of 0.001 °C for temperature and 0.01 psu (0.03 psu in strong thermocline regions) for salinity. The detailed specifications, sampling resolutions, and data processing procedures of the Seaglider are described in Jan et al. (2019) and Yang et al. (2023).

Two EM-APEX floats were deployed in the peripheral and center of 2024CE on 29 March 2024 (yearday 89) to measure temperature, salinity, and current velocity. Float f9749 was positioned at the center of the cyclonic eddy, while float f9750 was placed on its northwest side.

2.2 Flow cytometric analyses

To enumerate VIR, HB, PRO, SYNE, and PPE, 2 ml seawater samples from each depth were preserved with 0.5% paraformaldehyde (final concentration), flash-frozen, and stored in liquid nitrogen. In the laboratory, samples were analyzed using a Beckman Coulter CytoFLEX S flow cytometer (Indianapolis) equipped with a 488 nm argon-ion laser, a 525 nm filter, and a SYBR Green detection system. To reduce interference from high particle density, VIR samples were diluted 1:10 with TE buffer (pH 8.0, EM grade) prior to staining. SYBR Green I (final concentration 1:50,000) was added, and samples were incubated at 80 °C for 10 min in the dark. After staining, samples were cooled to 25 °C in an ice bath before analysis. Background noise was assessed by staining TE buffer alone. For HB enumeration, samples were stained with SYBR Green I (1:10,000 final concentration) for 15 min in the dark. Picophytoplankton populations (SYNE, PRO, and PPE) were distinguished based on red fluorescence (chlorophyll), orange fluorescence at 578 nm (phycoerythrin), and side scatter (SSC), following Calvo-Díaz and Morán (2006).

2.3 Atmospheric observations

The major instruments used for atmospheric observations include two types of radiosondes (Vaisala RS 41 and Storm Trackers), Micro Rain Radar-PRO (MRR-PRO), and a ceilometer. The RS 41 and ST radiosondes were

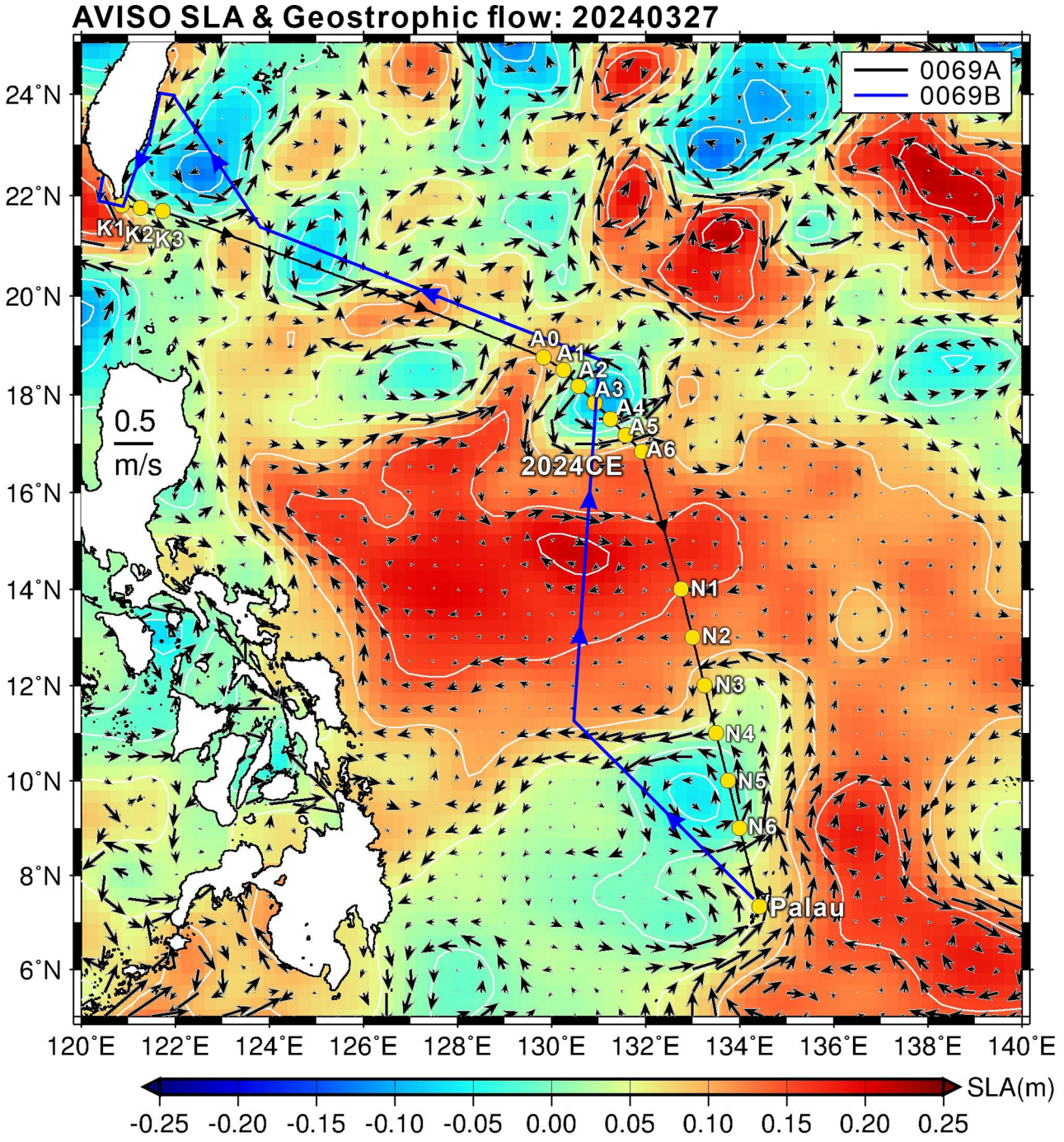

Fig. 3 Satellite sea level anomaly (SLA) and associated geostrophic flow anomalies (arrows) on 27 March 2024, and ship tracks of R/V New Ocean Researcher 1 cruise NOR1-0069 A (black line) and NOR1-0069B (blue line), and sampling stations (yellow filled circles)

released every 12 h (8 am and 8 pm local time) along ship track, additional ST radiosondes were released every 3 h in the eddy region (Table 1). The ceilometer observation was set at every 2 min.

The MRR-PRO enables us to assess operating atmospheric instruments on open data and provide foundational data for the upcoming shipborne C-band polarimetric radar (SPR). The MRR is a vertically pointing radar with frequency of 24.23 GHz. The radar transmitted frequency modulated continuous wave (FMCW) vertically upward. The hydrometeor above MRR scatters a portion of the energy back to the antenna. The magnitude and frequency of the backscatter signal provide the vertical profiles of reflectivity (Z_{HH}) and the Z_{HH} weighted fall velocity (V_Z).

Table 1 Ship-based and autonomous observations during the NOR1-0069 cruise

Observation	Instrument	Variables	Stations/period/dives
Ocean			
Hydrography	Seabird 911 plus	T, S, ρ, fluorescence, DO, transmission	16 stations (K1-K3; A0-A6; N1-N6. Coordinates are listed in Table 2.)
Biology	GoFlo bottles	Heterotrophic bacteria, Picophytoplankton communities, viruses	6 stations (A0-A6)
Surface (T, S)	Seabird SBE21 Thermosalinograph	T, S	Along ship track
Turbulence	VMP-250 micro structure sensor	TKE dissipation rates (ε)	6 stations (A0-A6)
Air-sea boundaries	SAFE T-bar	T_{air}, solar radiation (Sir), wind speed (w_x, w_y), sea surface temperature (SST), T proflies (upper 30 m)	9 days (2024/04/02-10)
Hydrography	Seaglider	T, S, ρ, fluorescence, dissolved oxygen (DO), light backscatter	309 dives (SG628 launched at A6)
Hydrography	EM-APEX	T, S, current velocity, surface wave spectra	f9750 and f9749 launched at A1 and A3, respectively.
Ground motion	CTTL	T and ground tilting	2023/10/09-2024/04/14
Gravity	SEA III Marine Gravity system	shipborne gravity	Along ship track
Atmosphere			
Underway wind anemometer		Speed (w_x, w_y)	
Radiosonde	Vaisala RS 41/Storm Tracker	u, v, T, humidity (q)	12 hourly (8 am and 8 pm local time) for the entire cruise; 3 hourly ST over cold eddy 2024CE region
Precipitation	Micro Rain Radar-PRO	Vertical profiles of reflectivity (Z_{HH}) and Z_{HH} weighted fall velocity (V_Z)	Along ship track
Ceilometer	Campbell SkyVUE8 (Lidar)	Cloud base heights and vertical visibility	Every 2 min along ship track
Underway meteorology	Ship-based meteorological sensors	T_{air}, humidity, solar radiation (Slr)	Along ship track

Table 2 Coordinate of sampling stations

Station	Longitude (°E)	Latitude (°*N*)	Notes
K1	120.8667	21.8010	
K2	121.2720	21.7522	
K3	121.7348	21.6860	
A0	129.8333	18.7500	
A1	130.2500	18.5000	Launch of EM-APEX f9750
A2	130.5833	18.1667	
A3	130.9167	17.8333	Launch of EM-APEX f9749
A4	131.2500	17.5000	
A5	131.5833	17.1667	
A6	131.9167	16.8333	Launch of Seaglider SG628
N1	132.7500	14.0000	
N2	133.0000	13.0000	
N3	133.2500	12.0000	
N4	133.5000	11.0000	
N5	133.7500	10.0000	Launch of SAFE T-bar
N6	134.0000	09.0000	

During the latter part of the cruise, MRR-PRO observations encountered interference issues, necessitating the development and application of data quality control (QC) procedures. After properly QC, a cell identification algorithm was applied to detect consecutive precipitation echo signals near the sea surface. The precipitation system thus can be obtained from the detected signals. Across the 26-day observation period, approximately 10.8% of MRR-PRO observations contained echo signals after a low signal-to-noise ratio (SNR) filter. The signal with low SNR is removed; however, some high-SNR data is still affected by electric interference. The precipitation identification algorithm eliminates the interference and detects 74 cells. The 74 cells account for approximately 1.6% of the total observation period. Figure 4 shows the daily distribution of detected signals and identified cells.

2.4 Seafloor ground-motion detection

Long-term monitoring of ground motions can provide constraints on seismic hazards and information of tectonic plate internal deformation. However, until recently, such monitoring for subwater areas has not been feasible, and little is known about the formation of oceanic crust or seamounts. In the vicinity of Taiwan—where two subduction systems merge—dense seismic activity and plate deformation occur as a result of plate convergence. In addition to seismic observations from land-based stations, we conducted a pioneering experiment to develop a stand-alone tiltmeter system to record seafloor ground motion in the eastern offshore area of Taiwan. The subwater tiltmetric recorder, integrated with small temperature loggers, was implemented in this study.

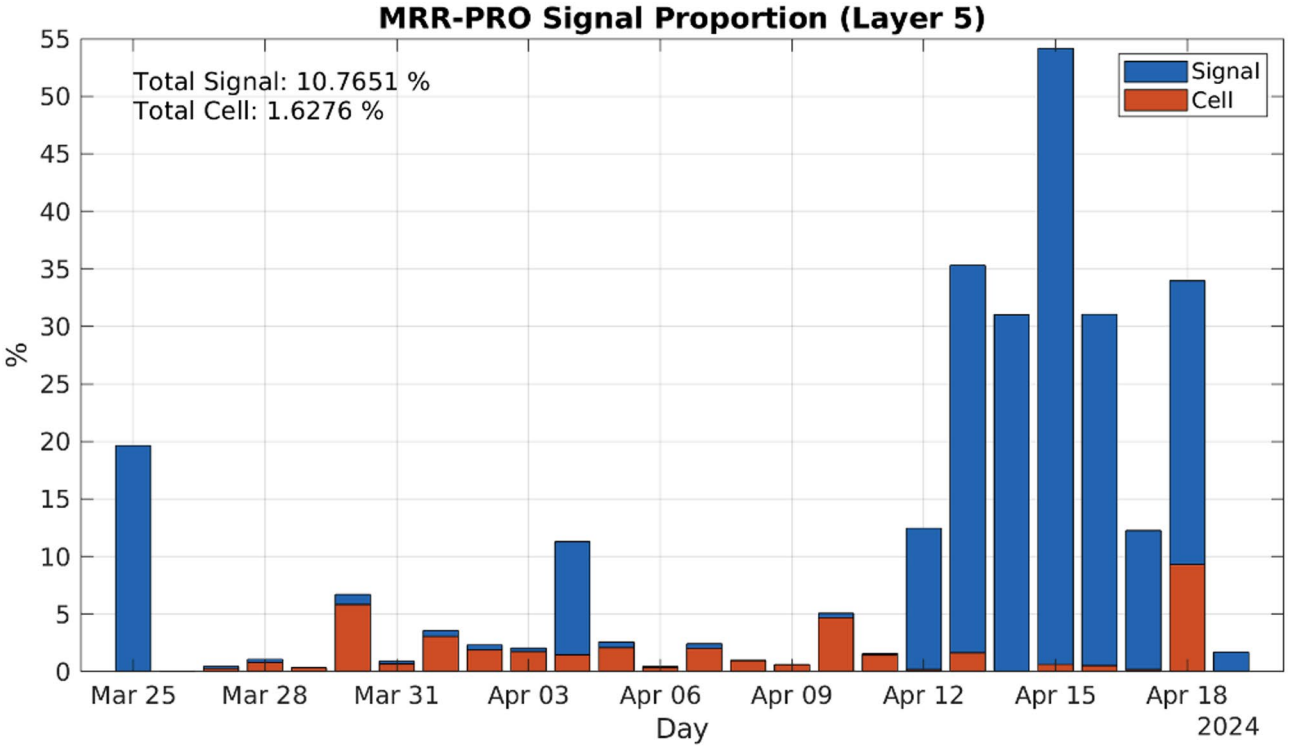

Fig. 4 Daily proportion of detected signals by MRR-PRO

These devices were originally designed to be attached to a solid steel lance on a core barrel in order to record temperature and attitude conditions during vertical sediment coring. During operation, frictional heat generated by transient penetration through the sediments is detected by the temperature logger. A pragmatic approach is to extrapolate a cylindrical temperature decay function to estimate the equilibrium ambient temperature and, therefore, to determine the heat conductivity of the sediments. To achieve rapid measurement of the ambient temperature, a 1-s sampling rate and a precision of 0.01 °C in the range of – 1 to 25 °C are required for the temperature logger. On the other hand, the tiltmetric sensor is designed to detect the gesture of the core barrel. Its recording precision is specified to be better than 1 degree; in this experiment, the resolution of the tiltmeter is approximately 0.05°. The electronic designs of these two sensors have been cleverly integrated and secured into a titanium cylinder measuring 22.2 cm by 2.2 cm, forming a compact tiltmeter with high-resolution temperature logger (CTTL). A detailed description of this device can be found in Chang and Shyu (2011). With a 24-bit, low noise analog to digital (A/D) converter embedded in the mix-signal microprocessor, both tiltmeter and temperature logger provide a highly stable reference for seafloor observation. The system is equipped with 4 MB of memory, allowing continuous operation for up to 16 days with a 1-s sampling interval. For lower sampling rates, such as a 1-min interval, the system can record continuous time series for up to one year.

In this experiment, two CTTLs (series numbers 351 and 352) were deployed as a stand-alone seafloor unit, employing an acoustic releaser to ensure recovery. The two CTTLs were mounted on a frame with a 50 cm height difference between the horizontal (351) and vertical (352) components. These devices stably recorded ambient water temperature and ground tilting every 30-s in the eastern limb of the Gagua Ridge (see location in the following text) from 9 October 2023 to 14 April 2024, covering a period of 188 days. This pioneering experiment successfully secured seafloor geophysical observations in the basin neighboring Taiwan. In particular, continuous seafloor ground-motion detection can provide significant insight into underwater ground motions and the geological processes interacting with deep water.

2.5 Along-track gravimetric observation

Although gravity models have been developed using satellite altimetry (Sandwell et al. 2014; https://topex.ucsd.edu/marine_grav/mar_grav.html), ship-based gr avity observations can provide a higher resolution for underwater areas. The gravimeter installed on NOR1 is an updated version of Micro-g LaCoste: SEA III Marine Gravity system. This new generation integrates the zero-length spring tension mechanism and a beam velocity sensor, and it is equipped with high-performance

gimbals. All of these features, along with a new slip-ring algorithm, create a robust and reliable platform for dynamic marine gravity survey. Detailed specifications for this device can be found at https://microglacoste.com/product/sea-iii-marine-gravity-system/.

During the long expedition across the entire Philippine Sea basin-from Kaohsiung Port (Taiwan) to Koror Port (Palau)-the along-track marine gravimetric survey provide a unique dataset for tectonic observation, particularly regarding in situ seafloor topographic feature in the deep sea (exceeding 6000 m in depth). The initial offset of the gravity anomaly was determined by comparing data from a local station near Kaohsiung Port (Site G112, 120.2989°E 22.6225°N) and the onboard measurements. The calibration of the tidal models has been taken from the tidal gauges at ports and global tidal models for the open ocean (https://www.tpxo.net/global). The system provided continuous gravity survey data at a 1-s sampling rate from 8 to 15 April 2024 during NOR1-0069B.

3 Results

3.1 Hydrography in the eddy and across the Kuroshio and NEC

Figure 5 shows temperature, salinity, and density (σ_t) across the 2024CE (stations A0-A6). The hydrography transects of this eddy present typical characteristics of a cold-core eddy. Pronounced isotherms uplift is observed approximately in the upper 400 m of the eddy center (around A3 and A4; Figs. 5a, b) with a vertical displacement of 15–20 m between 100 and 200 m depths (Fig. 5a). The temperature in the eddy center is ~2℃ lower than the temperature in the surrounding area. The σ_t profiles (Figs. 5e, f) present similar patterns to the temperature profiles. The isotherms and isopycnals also show that their slopes are higher in the southeast than in the northwest quadrant of the 2024CE (Fig. 5a, e), which indicate stronger northeastward-flowing eddy current in the southeast portion of the eddy (see satellite geostrophic current anomalies related to this eddy in Fig. 3). The salinity profiles (Fig. 5c, d) show that the salinity maximum and minimum range approximately between 140 m and 180 m and between 500 m and 600 m depths, respectively.

The concurrently measured profiles of turbulence kinetic energy dissipation rates (ε) at the seven stations are plotted over the upper 300 m temperature transect in Fig. 6. In general, ε reached 10^{-7}-10^{-6} W kg^{-1} near the surface (upper 20 m), while was < 10^{-9} W kg^{-1} in the other depths. The range of ε in the upper ~ 250 m remains as its typical value for an eddy in the open ocean.

The water masses across the Kuroshio (stations K1-K3), 2024CE, and the NEC (stations N1-N6) are illustrated in the T-S diagram shown in Fig. 7. In the western boundary of the North Pacific, water masses are dominated by North Pacific Water (NPW; also called Philippine Sea Water), Kuroshio-origin Water (KW), and South China Sea Water (SCSW) (Mensah et al. 2014, 2015). It is clear that water masses in this region are complex. At the three stations across the Kuroshio of the southern tip of Taiwan, K1 and K2 present SCSTW/NPTW mixed water in

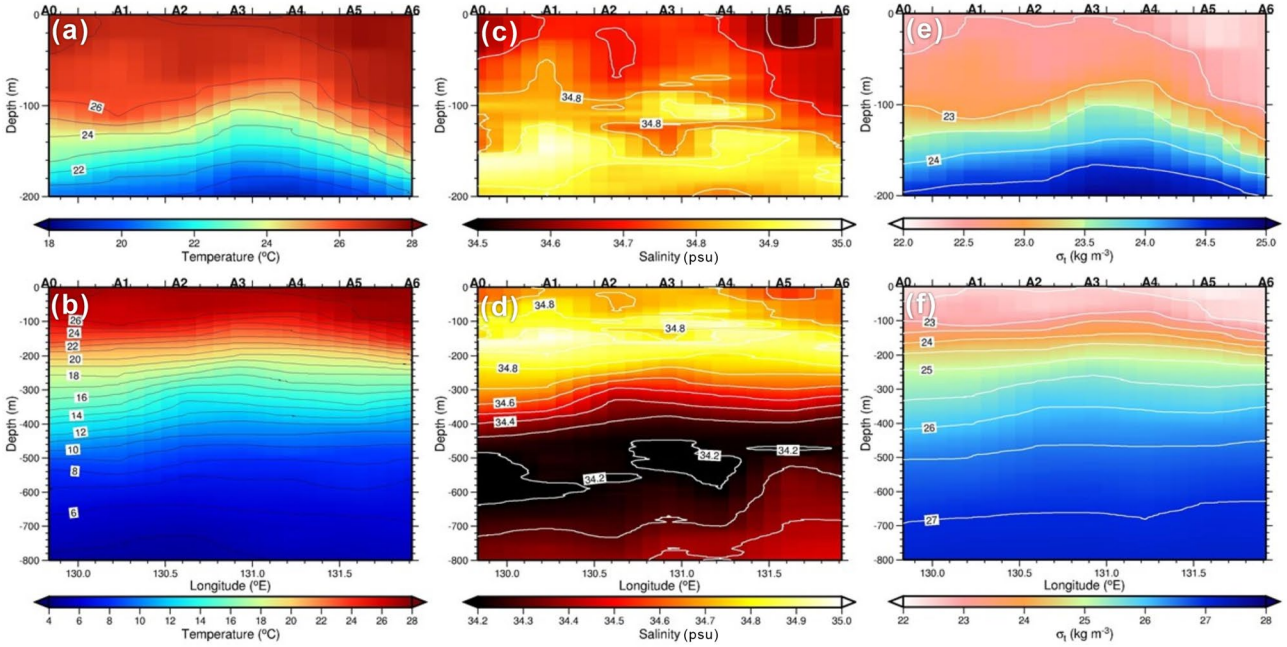

Fig. 5 Hydrographic transects across the 2024CE obtained from the ship-based CTD observations. Panels show detailed view of the upper 200 m and 0-800 m sections of (**a, b**) temperature, (**c, d**) salinity, and (**e, f**) density (σ_t)

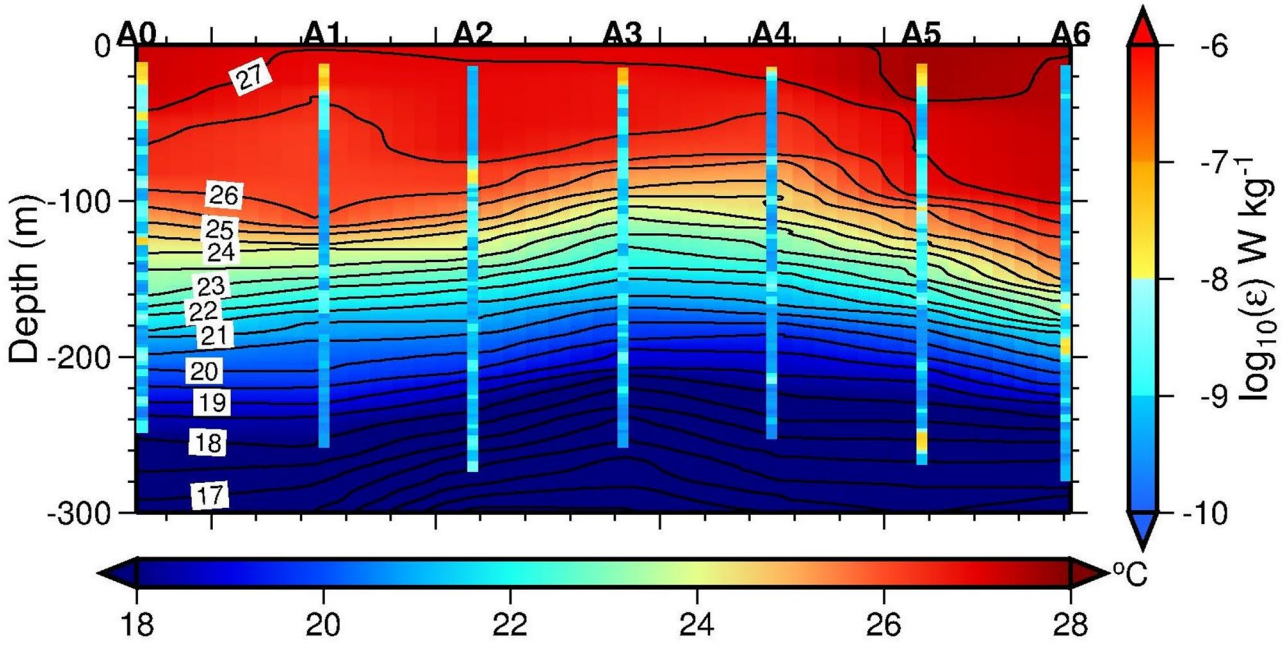

Fig. 6 Profiles of turbulence kinetic energy dissipation rate (ε) at seven hydrographic stations across the 2024CE. The ε profiles are superimposed on the temperature transect in the upper 300 m to illustrate the vertical structure of turbulence relative to thermal stratification

the tropical water layer and KIW/SCSIW mixed water in the intermediate water layer. In contrast, K3 exhibits characteristics of a mixture between NPTW and KIW/NPIW. Water masses in the 2024CE were consist of NPTW/KTW mixed water and NPIW below. Further to the south, water masses at 14°N was likely the Kuroshio origin water; KTW and KIW. At 13°N, the tropical water mass became KTW/NPTW mixed water and the intermediate water varied between KIW and SCSIW. The tropical and intermediate water masses at 9°-12°N stations were NPTW and SCSIW-like water, respectively.

In comparison with the ship-based CTD observations (Fig. 5), the Seaglider observations provide more detailed hydrographic features of the 2024CE. Figure 8 shows the Seaglider's trajectory and the observed temperature and salinity profiles across the 2024CE. Note that the Seaglider sampled the hydrography profiles at intervals of approximately 4 h each dive, with each dive consisting of a descending and an ascending profile. Therefore, two profiles were observed within approximately 4 h. Although this sampling rate is only slightly higher than the Nyquist frequency for semidiurnal tides, it is sufficient for resolving the vertical displacements of isotherms induced by internal tides. The sampling from 30 March to 16 April 2024 crossed the southeast of the 2024CE (cf. satellite SLA in Figs. 8a, b) and the temperature transect (Fig. 8c) shows tidally-induced internal vertical oscillations overlaid on the heaved isopycnals, particularly within 60 and 120 m depths around the center of the 2024CE (~131.35°E in Fig. 8a). Similar to Fig. 8c, the salinity transect (Fig. 8d) shows various depth of salinity maximum (within 120 and 150 m) and minimum (within 500 and 600 m) under the influence of the eddy. To highlight the eddy-induced isotherm heave, Fig. 8f shows a close-up of the upper 300 m temperature profiles across the eddy. Despite the presence of tidally-induced oscillations, the isotherm displacements between 60 and 120 m depths were approximately 40–50 m, consistent with those shown in Fig. 6. The dissolved oxygen (DO) concentration (Fig. 8e) shows spatial variability between 200 and 400 m. A low DO zone is observed near the southeast boundary of the cyclonic eddy, compared with relative high zones outside and in the center of the eddy.

Observations from the two EM-APEX floats (Fig. 9) complemented the hydrographic mapping of the 2024CE. The isopycnal of $\sigma = 23$ kg m^{-3} at float f9749 was 70 m shallower than that at float f9750, consistent with the expected spatial variation of ocean structure within a cyclonic eddy. As a result, the upper 100-m ocean stratification, identified by using the buoyancy frequency N^2, was stronger at the eddy's center than at its periphery. The salinity below 100-m depth at float f9750 was higher than that at float f9749 (Figs. 9c and i), yielding different T-S properties between the center and the edge of the eddy. After deployment, float f9750 might drift southwestward due to the strong geostrophic current. Both floats recorded strong semi-diurnal tides. The shallowest measurements at about 2.5-m depth was used as the sea surface temperature (Hsu et al. 2024). On both floats, the nighttime SST (at ~00:00 UTC) was similar on

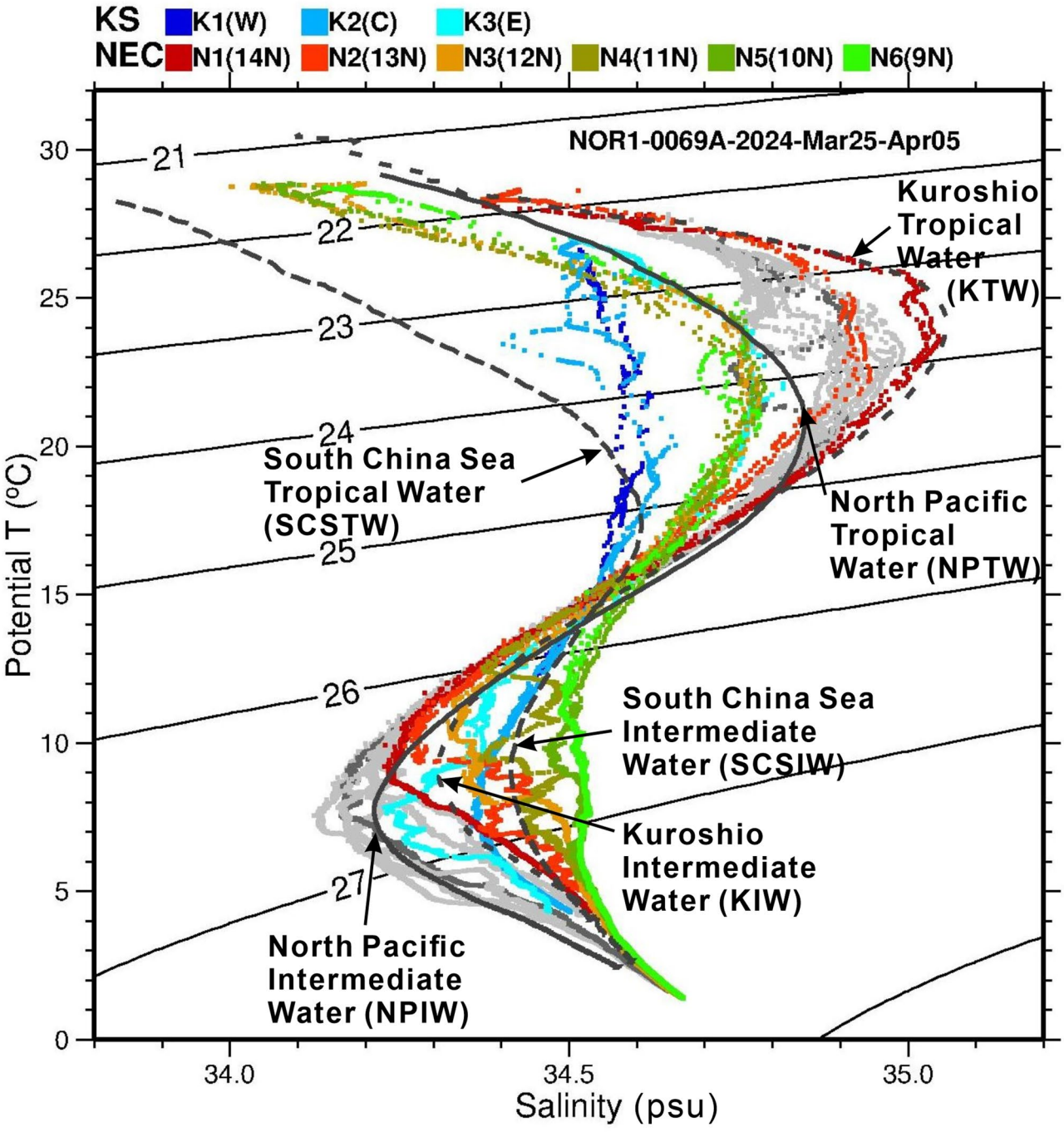

Fig. 7 T-S diagram of hydrographic data collected from CTD stations across the Kuroshio (K1-K3, colored dots), NEC (N1-N6, colored dots), and the 2024CE (gray dots). For reference, mean T–S curves representing tropical and intermediate waters from the South China Sea, North Pacific, and Kuroshio origin (as documented in Mensah et al. 2014; 2015) are overlaid

yearday 89 but increased until yearday 92, with a more pronounced warming at float f9750 than at float f9749 (Figs. 9b and h). According to the COARE algorithm (Fairall et al. 2003), the SST changes can directly enhance the air-sea heat fluxes, thereby the heat and moisture in the atmosphere boundary layer (Hsu et al. 2022). Further analysis is needed to identify the factors driving the differences in SST warming between the two floats.

3.2 Biological properties in the 2024CE

3.2.1 Vertical distribution of picophytoplankton

Table 3 lists vertical distribution of SYNE, PRO, PE, HB, and VIR at stations A0-A6. PRO was the predominant

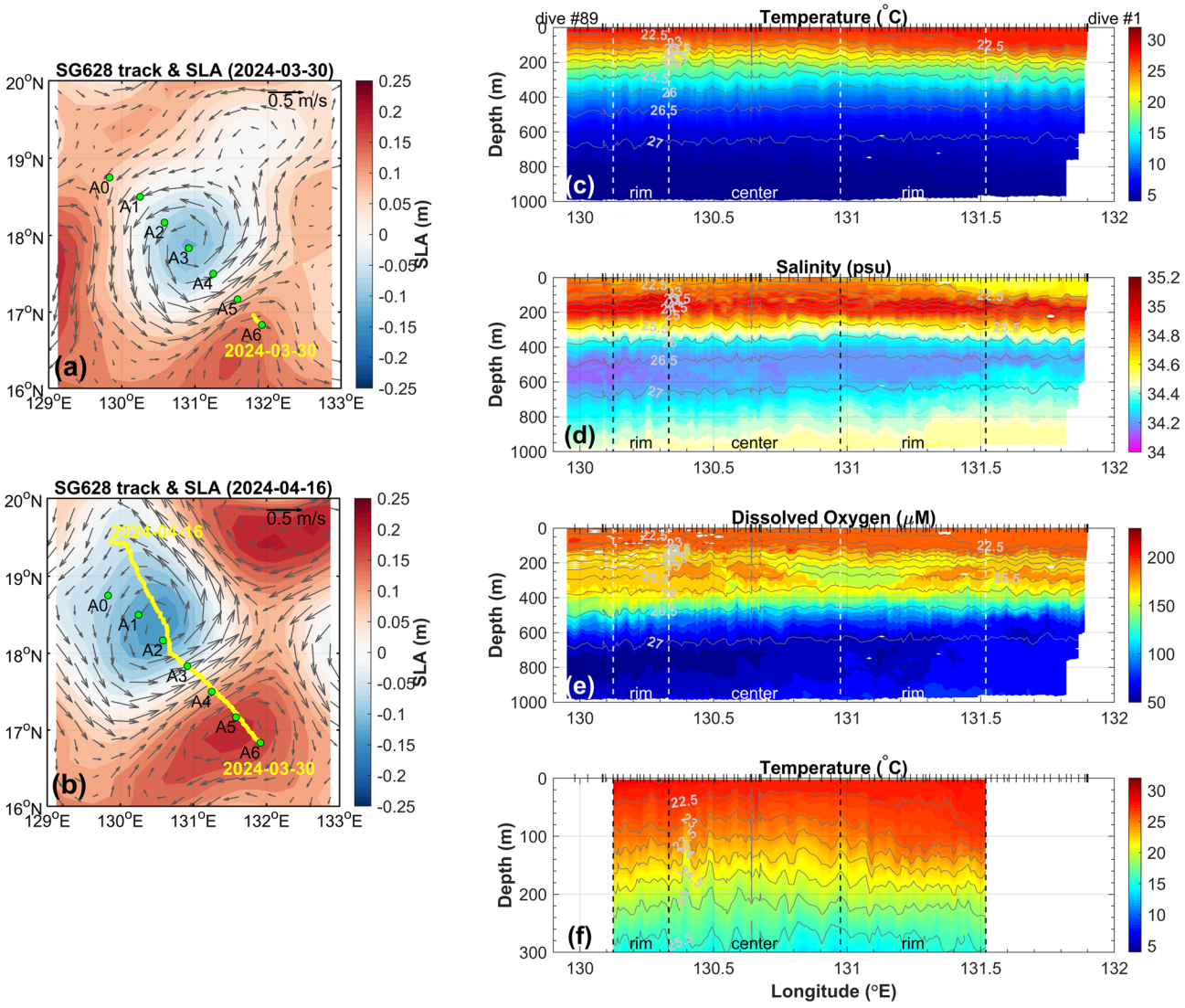

Fig. 8 Hydrographic observations from Seaglider SG628: satellite SLA and geostrophic velocity anomalies (arrows) on (**a**) 30 March 2024 and (**b**) 16 April 2024 with glider trajectory (yellow line), (**c**) temperature, (**d**) salinity, and (**e**) dissolved oxygen concentration with isopycnal contours. (**f**) A close-up of the upper 300 m temperature profiles across the cyclonic eddy

picophytoplankton throughout the cold eddy, whereas the abundance of SYNE was typically an order of magnitude lower than that of PRO at depths shallower than 100 m. At all stations, however, SYNE abundance was higher than PRO abundance below 200 m to 1000 m (Table 3). Overall, the abundance of SYNE and PRO was high within 100 m depth, declining with depth and becoming extremely low at all stations. Outside the cold eddy (stations A0, A1, and A5), the vertical distributions of SYNE and PRO were correlated with both temperature and salinity ($r = 0.58$, 0.50 for SYNE; $r = 0.65$, 0.56 for PRO, respectively). However, within the cold eddy (stations A2, A3, and A4), SYNE and PRO were correlated with temperature ($r = 0.47$ and $r = 0.70$, respectively) but not with salinity.

In addition to SYNE and PRO, the vertical distribution of picoeukaryotes (PE) was assessed. Interestingly, PE exhibited a distinct pattern compared to the cyanobacterial groups. Maxima in PE abundance were consistently observed at intermediate depths between 100 and 200 m, particularly at stations A2, A3, and A4, which were influenced by the cold eddy (Table 3). Moreover, vertical profiles of PE within the euphotic zone were found to be highly influenced by the cold eddy, due to higher values observed at A2, A3, and A4. Among the picophytoplankton groups, PRO was the dominant taxon in the upper water column, contributing between 62% and 95% of total picophytoplankton abundance above 100 m in cold eddy-influenced regions (Table 3). The vertical profile of PRO contribution showed a pronounced peak at approximately 100 m, followed by a decline with increasing

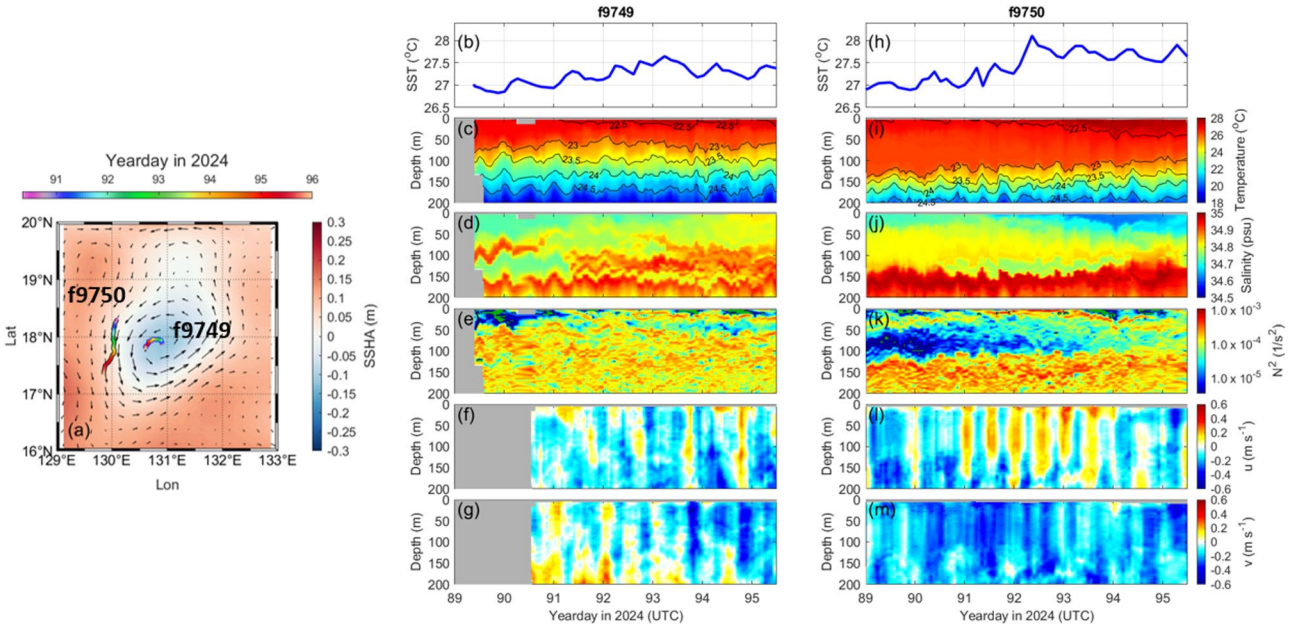

Fig. 9 Trajectories of two EM-APEX floats (color dots marked by the horizontal color bar in (**a**) and sea surface height anomalies of the cold eddy (color shading shown by vertical color bar in **a**). Data of f9749 (left column) and f9750 (right column) are shown in (**b**)-(**m**), including sea surface temperature (**b**) and (**h**), upper 200 m temperature (**c**) and (**i**), salinity (**d**) and (**j**), buoyancy frequency squared (**e**) and (**k**), zonal current velocity (**f**) and (**l**), meridional current velocity (**g**) and (**m**)

depth. At stations A2, A3, and A4, a secondary peak in PRO percentage was observed at depths of 300–400 m, resulting in an S-shaped vertical variation (Table 3).

3.2.2 Vertical distribution of bacteria and virus

The HB abundance also revealed spatial and depth-dependent variations. As shown in Table 3, across all stations, higher concentrations of HB were observed in the upper 200 m. Surface HB abundances were typically around 2×10^5 cells mL^{-1}, increasing with depth at most locations. At stations A0, A1, A4, and A5, bacterial abundance peaked near 200 m, exceeding 4×10^5 cells mL^{-1}. In contrast, at stations A2 and A3, which were influenced by the cold eddy, maximum bacterial concentrations occurred at much shallower depths, around 50 m. For VIR, no consistent vertical feature was detected across stations (Table 3). Like picophytoplankton, outside the cold eddy (at stations A0, A1, and A5), the vertical distribution of HB showed correlations with both temperature and salinity ($r = 0.54$ and $r = 0.69$, respectively). In contrast, inside the cold eddy (stations A2, A3, and A4), HB was correlated with temperature ($r = 0.71$) but showed no correlation with salinity. Additionally, VIR did not exhibit any correlation with either temperature or salinity.

3.3 Geophysical aspects

3.3.1 Potential seafloor ground motions detected at CTTLs

The two CTTLs functioned as a stand-alone ground motion detector, freely falling and settling on the seafloor after being launched from the research vessel at the planned site. The time series of ambient water temperature and ground tilting are presented in Fig. 10, showing clear temporal trends. Notably, the temperature records from the two individual CTTLs exhibit similar time series, suggesting that the observed temporal variations are not trivial electrical baseline drifts. From October 2023 to April 2024, the ambient water temperature at the site varied from 1.42 °C to 1.44 °C, with a tiny increase of 0.02 °C. Additionally, the temperature data reveal distinct oscillations corresponding to the diurnal tidal period.

Due to the uneven landing surface, the initial angles after settling into the sediments were 27.25° and 94.75° for the vertical and horizontal components, respectively. Unlike the relatively stable temperature series, the seafloor tilting data at both CTTLs exhibit an interesting pattern. Over four months, both tiltmeter time series display a linear shift before experiencing two distinct baseline jumps, which occurred on 9 February at 06:21 and 12 February at 09:42, respectively. Similar to the inference drawn from the temperature time series, these deviations occurred simultaneously in these two individual tiltmetric measurements, leading us to attribute them to seafloor ground motion or geological processes affecting ground stability. In parallel, the temperature time series also show a small but noticeable disturbance from 9 to 12 February. We infer that the detected ground motion was minor and did not cause significant disturbances in the bottom sediments or ambient water. Before

Table 3 Vertical distribution of SYNE, PRO, PE, HB, and VIR at stations A0-A6

St. A0		SYNE	PRO	PE	HB	VIR
	depth	(10^3 cells mL^{-1})	(10^3 cells mL^{-1})	(10^3 cells mL^{-1})	(10^5 cells mL^{-1})	(10^6 viruses mL^{-1})
	5	5.96	12.90	0.00	1.37	4.73
	10	4.62	11.52	0.00	1.71	4.33
	25	5.73	9.52	0.00	1.53	2.56
	50	4.99	25.88	0.00	1.90	3.90
	75	5.40	54.61	0.00	1.92	4.62
	100	6.57	69.30	0.00	1.97	4.10
	200	2.29	1.16	0.00	4.04	4.19
	300	2.36	1.46	0.00	1.59	4.46
	400	2.29	0.83	0.00	1.29	3.31
	600	2.44	0.90	0.00	1.17	3.63
	800	2.47	0.00	0.00	0.59	0.60
	1000	4.99	0.00	0.00	0.47	0.86
St. A1						
	5	12.98	21.98	0.08	2.01	0.85
	10	8.91	20.24	0.00	2.04	0.70
	25	13.16	23.44	0.04	2.13	0.62
	50	14.89	40.65	0.00	3.02	0.45
	75	11.40	49.95	0.11	2.20	0.68
	100	12.89	69.38	0.11	2.10	0.56
	200	3.90	0.90	0.08	3.76	0.60
	300	1.91	0.41	0.00	0.30	0.85
	400	4.27	0.98	0.00	0.44	1.19
	500	3.49	0.53	0.00	0.29	1.27
	600	3.64	0.98	0.00	0.65	0.58
	800	3.90	0.90	0.00	1.28	1.40
	1000	7.84		0.49	0.42	1.08
St. A2						
	5	8.44	16.77	0.16	2.04	1.03
	10	5.93	14.22	0.04	1.45	0.81
	25	10.54	21.64	0.04	1.91	1.26
	50	7.28	28.62	0.04	1.68	0.97
	75	9.87	56.40	0.12	1.87	1.50
	100	7.84	54.34	0.19	1.49	0.74
	200	2.67	1.43	0.49	0.39	1.60
	300	3.34	0.45	0.04	0.32	0.52
	400	3.90	0.75	0.00	0.23	0.48
	600	1.39	1.39	0.00	0.14	0.44
	800	1.42	1.39	0.00	0.13	0.71
	1000	2.10	1.06	0.00	0.14	1.04
St. A3						
	5	4.39	17.29	0.04	2.07	0.85
	10	2.44	17.63	0.04	2.16	1.11
	25	4.54	28.09	0.00	2.78	0.74
	50	4.39	31.43	0.04	2.18	0.91
	75	2.78	36.42	0.00	2.00	0.95
	100	1.73	29.70	0.68	1.50	0.95
	200	2.21	0.94	0.04	0.52	0.85
	300	1.39	1.73	0.00	0.28	1.00
	400	1.65	1.05	0.00	0.27	0.82
	500	2.14	0.04	0.00	0.30	1.21
	800	4.69	0.11	0.00	0.16	0.70
	1000	2.93	0.04	0.00	0.15	0.87

Table 3 (continued)

St. A0		SYNE	PRO	PE	HB	VIR
	depth	(10^3 cells mL^{-1})	(10^3 cells mL^{-1})	(10^3 cells mL^{-1})	(10^5 cells mL^{-1})	(10^6 viruses mL^{-1})
St. A4						
	5	0.87	20.22	0.00	2.70	0.78
	10	1.05	19.92	0.00	2.93	1.38
	25	1.09	13.99	0.11	2.79	0.93
	50	1.80	15.60	0.11	2.63	0.88
	75	2.97	53.22	0.19	1.67	0.53
	100	4.05	43.58	0.42	2.09	0.77
	200	0.64	0.19	0.00	4.34	0.85
	300	0.23	0.23	0.00	2.11	0.93
	400	0.12	0.30	0.00	2.27	1.95
	600	0.45	0.49	0.00	2.24	0.99
	800	0.34	0.08	0.00	0.86	1.54
	1000	0.38	0.27	0.00	0.80	1.13
St. A5						
	5	5.93	19.95	0.00	2.48	0.61
	10	4.13	10.09	0.04	1.54	1.53
	25	6.91	21.08	0.04	1.99	1.87
	50	9.00	32.44	0.08	2.61	2.95
	75	9.90	36.08	0.04	1.97	2.70
	100	6.57	71.27	0.04	2.03	1.89
	200	4.62	3.60	0.15	4.99	2.16
	300	4.35	1.61	0.04	2.58	3.03
	400	3.27	1.09	0.00	1.69	2.27
	600	2.55	0.86	0.00	1.72	2.67
	800	3.00	0.86	0.00	0.93	3.02
	1000	2.14	0.87	0.00	0.70	3.68
St. A6						
	5	11.63	13.46	0.00	2.01	3.80
	10	8.57	14.86	0.00	1.66	4.03
	25	10.50	19.20	0.00	1.83	4.05
	50	8.59	28.28	0.08	1.98	4.59
	75	12.31	38.85	0.00	1.70	4.93
	200	5.29	3.75	3.53	0.52	4.93
	300	3.94	2.74	0.00	0.41	4.44
	400	2.25	2.47	0.00	0.33	4.35
	600	3.15	1.96	0.00	0.22	4.54
	800	1.84	1.88	0.00	0.14	4.41
	1000	2.96	1.84	0.00	0.16	3.58

and after the baseline jumps, the tilting trends differed at these two tiltmeter time series, further indicating the dynamic nature of seafloor ground motions. These data demonstrate the feasibility of detecting seafloor ground motion through an integrated tiltmeter and temperature logger system. Moving forward, we aim to refine the system's design to enhance the resolution of tilting detection (currently ~ 0.05°) and achieve more precise quantitative measurements of seafloor ground motion.

3.3.2 Shipborne gravity anomaly across the Philippine sea basin

The shipborne gravity data were collected (at a rate of 1 Hz) from Koror Port, Palau, to Kaohsiung Port, Taiwan, between 8 and 17 April 2024, covering a distance of approximately 3,000 km across the Philippine Sea Basin. Figure 11 presents the gravity anomaly measured along the ship's track from April 9 to 15, 2024, with nearshore data removed.

During the cruise, the ship's track was set to recover marine instruments deployed in previous experiments. The sailing route crossed over oceanic spreading ridges and fracture zone faults multiple times. As marine

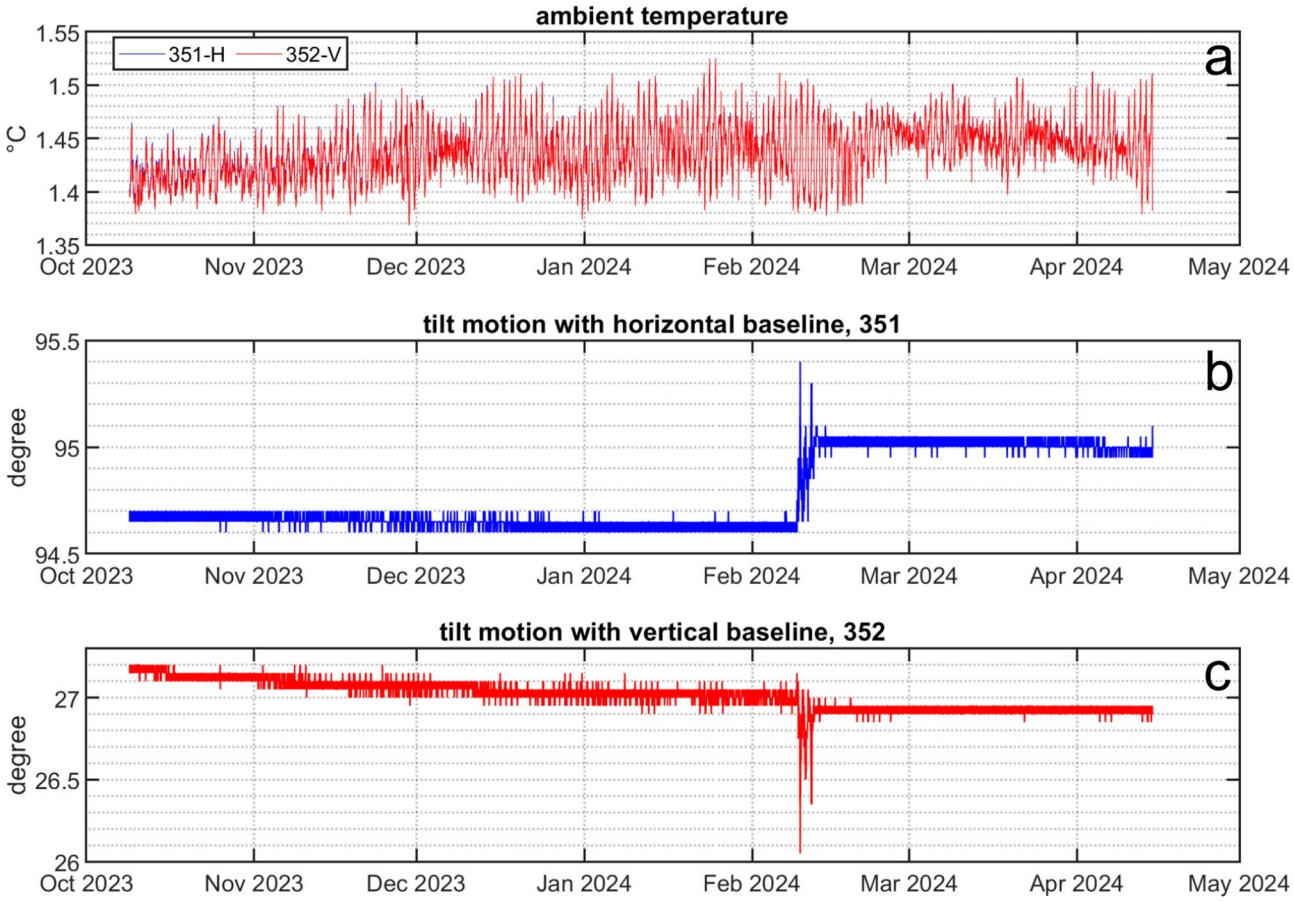

Fig. 10 Time series of the CTTLs retrieved from the seafloor station east of the Gagua Ridge. (**a**) Temperature time series at two CTTLs. The two temperature records are similar, resulting in an overlapping plot in the panel. (**b**) and (**c**) Tiltmeter time series at 351 and 352. Two baseline jumps occurred simultaneously in both tiltmeters

gravity data can provide important constraints on the density structure of the lithosphere, these observations are important to advance the discussion of the ridge formation and the material distribution over the plate divergent zone. The ongoing study with these observations has been structured to combine with satellite altimetry data to provide the heterogeneity of ocean crust over the ridges. The gravity anomaly data shown in Fig. 11 represent a combined plot of along-track measurements. The vertical lines in Fig. 11b serve as markers indicating the accumulated distances where instrument recovery operations took place.

For comparison, the bathymetric profile was also provided along the gravity survey track. The bathymetric profile was extracted from the global ocean data bank, General Bathymetric Chart of the Oceans (GEBCO https://www.gebco.net/), which provides data on a 15' grid interval (Fig. 11a). The bathymetric profile shown in Fig. 11b was resampled using the Generic Mapping Tool (GMT) function "grdtrack". The vertical lines in Fig. 11b serve as markers indicating the accumulated distances where instrument recovery operations took place (red circles in Fig. 11a).

3.4 Atmospheric observations over the Western North Pacific

In terms of the observation of the lower atmospheric boundary layer (ABL) during NOR1-0069, the MRR, radio sounding, and ceilometer continuously collected valuable measurements over the northwest Pacific. The sounding provides environmental conditions, including ABL height, atmospheric instability, inversion layer height, and moisture vertical distribution, among other factors determining the atmospheric conditions. The ceilometer provides the cloud cover and cloud height. The MRR measured the precipitation profile above the sailing NOR1. The precipitation cell identification algorithm provided critical parameters for each detected precipitation cell, including maximum reflectivity and echo top height, as determined by MRR. By considering the ship motion, the precipitation cells' spatial characteristics were also estimated. Results indicate that most cells had limited vertical development, with echo tops generally

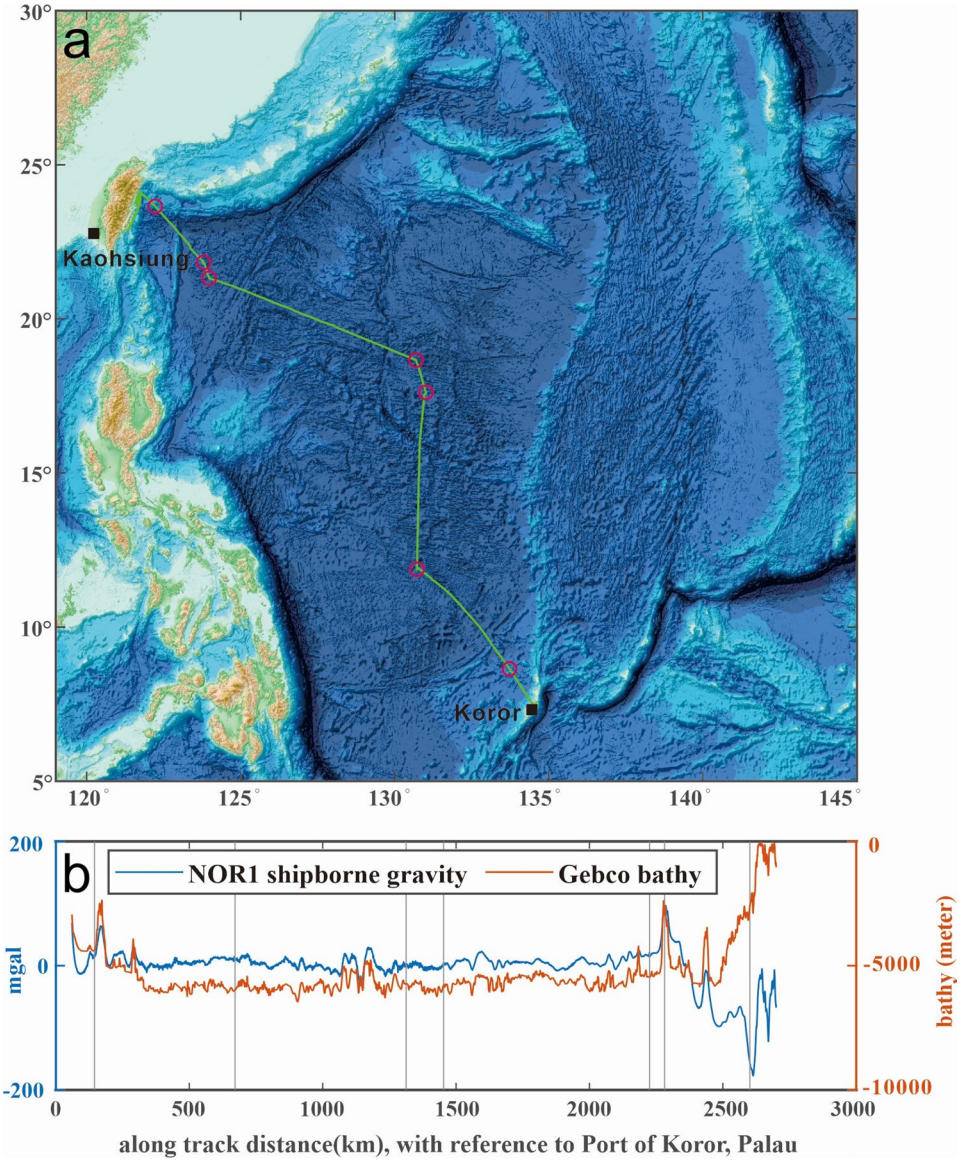

Fig. 11 The along-track shipborne gravity anomaly. (**a**) The track line across the Philippine Sea Basin, with turning points indicated as red circles. (**b**) The surveyed gravity data are plotted alongside the topographic profile obtained from the GEBCO database along the track. The distance was measured along the track from Koror Port. The vertical black lines indicate the positions of the turning points (red circles in (**a**)) in sequence

below 3 km and cell sizes not exceeding 2.5 km. Figure 12 illustrates the relationship between precipitation cell properties, revealing a positive correlation between echo top height and maximum reflectivity.

Figure 13 illustrates the echo tops of detected cells alongside the track of NOR1. The precipitation cells are more vigorous in tropical regions, with higher echo tops. While the MRR-PRO does not provide dual-polarimetric measurements, the data can retrieve the Drop Size Distribution (DSD) by applying the relationship between the terminal fall velocity and the diameter of raindrops. Figure 14 presents a time-series profile of reflectivity (Fig. 14a), low-level DSD (Fig. 14b), and associated meteorological parameters (Figs. 14c-e) for a selected precipitation cell (i.e., identified cell #48). The accumulated precipitation estimated from both MRR-PRO and IMERG (Integrated Multi-satellitE Retrievals for GPM) is also included in Fig. 14a. In this case study, moderate reflectivity values (20-30 dBZ) are found near the cell's core (Fig. 14a), indicating areas of significant precipitation. The DSDs reveal the possible presence of larger raindrops (up to 7 mm). Nevertheless, the majority of the raindrops were less than 3 mm in size.

As the precipitation cell passes, there is a noticeable decrease in air temperature (Fig. 14c) and solar radiation (Fig. 14d), accompanied by a drop in wind speed (Fig. 14d). The sounding profile collected before the cell's passage indicates the environmental limitation on

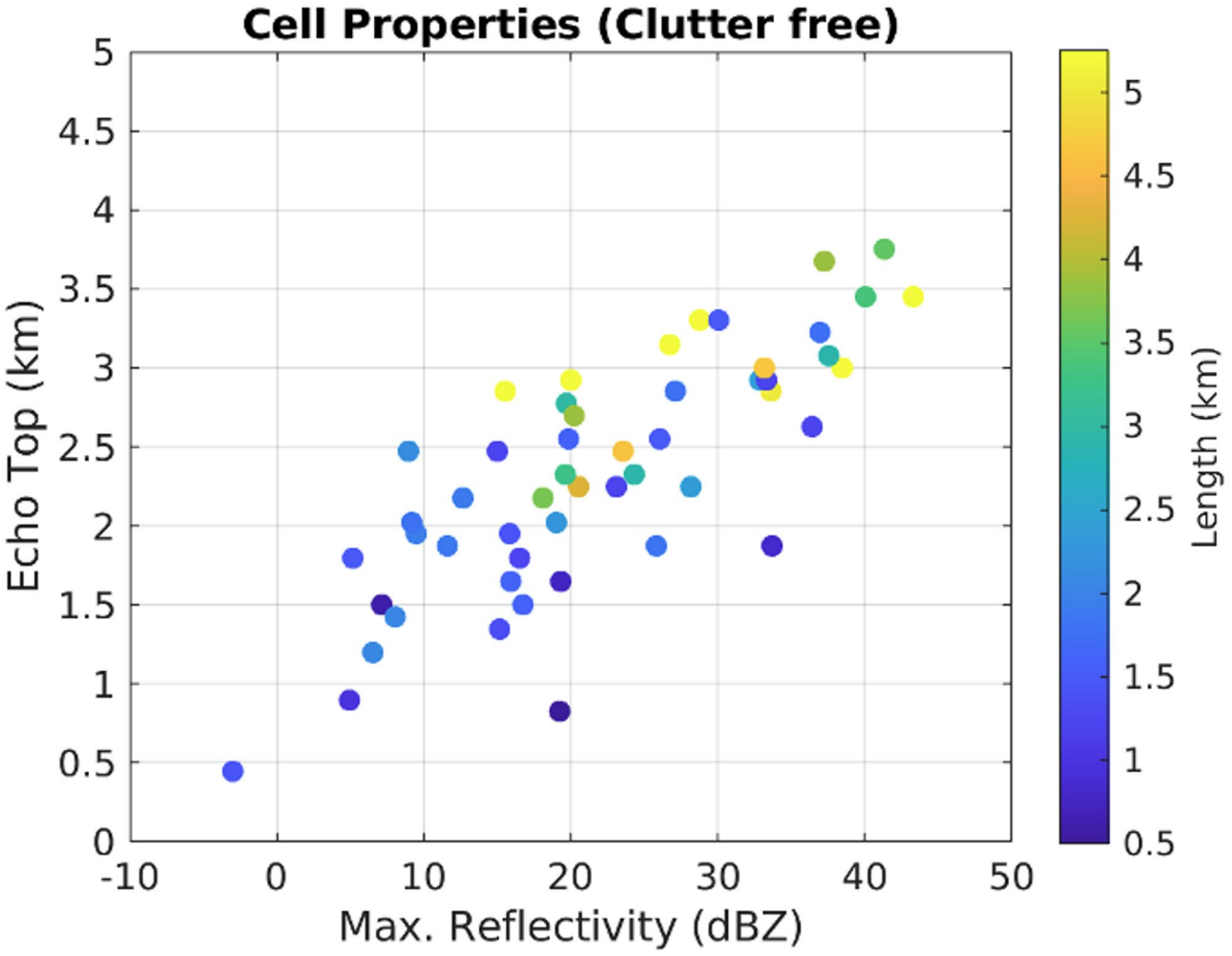

Fig. 12 Scatter plot of cell properties including maximum reflectivity (x-axis, dBZ) and echo top of identified cell (y-axis, km). The shaded color indicates the length of the identified cell

convection development. A temperature inversion layer with high discrepancy between the dew point and environmental temperature (green and red lines in Fig. 14f) is observed at approximately 700 hPa (~ 3 km). The discrepancy aligns with the echo top of the convection. The dry layer above the inversion likely suppresses the positive buoyancy within the convection through entrainment effects, limiting the vertical extent of convection.

Figure 15 illustrates the probability density function of rain rate (x-axis) and reflectivity (y-axis) at the lower levels of identified precipitation cells. Preliminary analysis shows higher rain rates for a given reflectivity in maritime shallow convection than continental convection, suggesting smaller raindrop sizes in maritime environments.

In addition to the MRR precipitation measurements, the ceilometer provides the cloud properties over the maritime environments. Figure 16 shows the backscatter and cloud cover data from the NOR1-0069 cruise. The pronounced diurnal signal is evident in the backscatter measurements of the ceilometer. The cloud cover is consistent with the MRR measurements. The precipitation period observed by MRR has lower cloud cover, indicated by the ceilometer.

4 Summary and discussion

The NOR1-0069 cruise carried out an interdisciplinary campaign involving physical and biological oceanography, marine geophysics, and atmospheric observations across the western North Pacific, along a transect between Taiwan and Palau. The combination of ship-based and autonomous underwater observations provides valuable insight into the physical, biological, and biogeochemical properties of the 2024CE centered at (131°E, 18°N) and its role in modulating air-sea interactions and oceanic weather. The hydrographic data shown in the T-S diagram indicate that the water masses on the western and eastern flanks of the Kuroshio off the southeastern Taiwan were basically composed of South

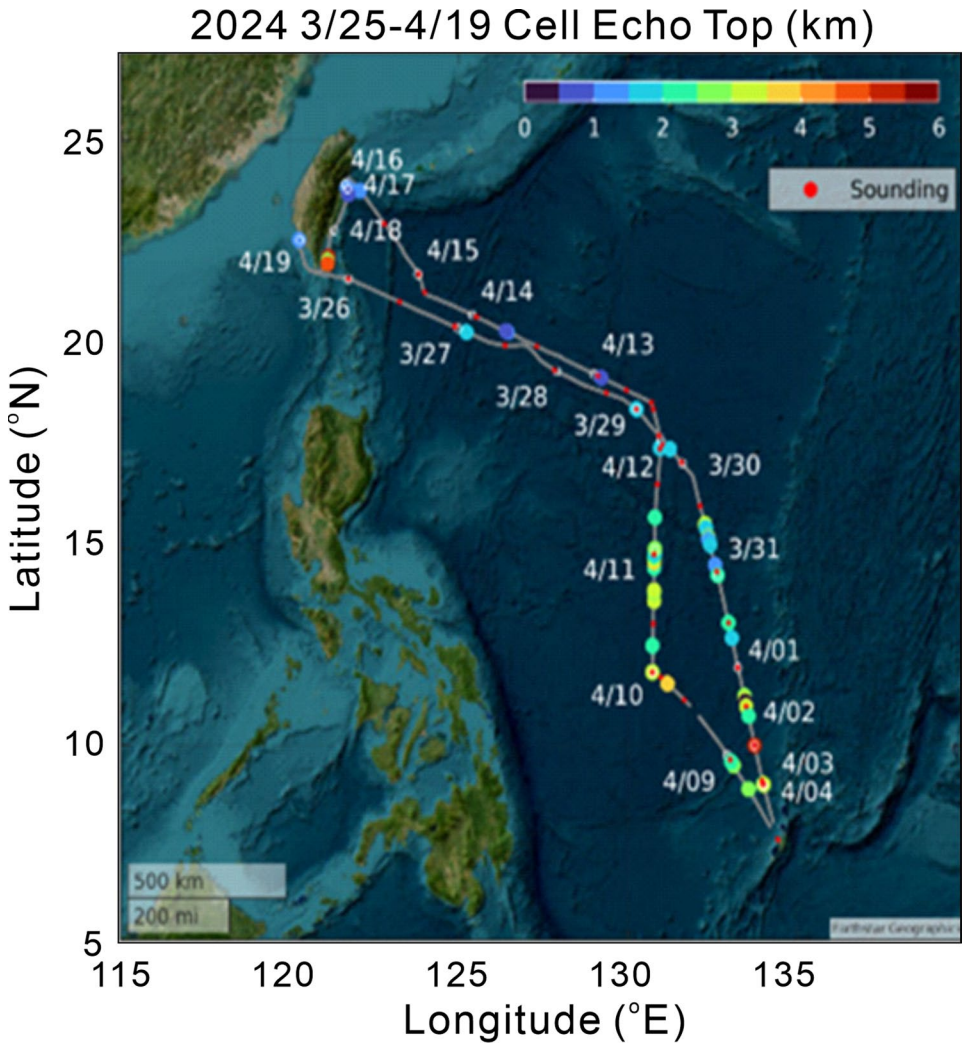

Fig. 13 Geolocation of cells colored with echo top height

China Sea Water and North Pacific Water, respectively. The 2024CE was mostly characterized by North Pacific Water. Across the NEC, the water masses consisted of North Pacific Water and Kuroshio-origin North Equatorial Current Water. Within the 2024CE, the turbulence kinetic energy dissipation rate reached 10^{-7}-10^{-6} W kg^{-1} in the upper 20 m, decreasing to smaller than 10^{-9} W kg^{-1} at deeper depths.

Biological sampling within the 2024CE revealed regionally distinct patterns influenced by the cyclonic eddy. Stations A3 and A4 showed the lowest peak abundances of SYNE and PRO, while PE concentrations exceeded 0.4×10^3 cells mL^{-1} at depths between 100 and 200 m at A2-A4. HB abundance increased from approximately 2×10^5 cells mL^{-1} at the surface to over 4×10^5 cells mL^{-1} at 200 m at A0, A1, A4, and A5, with additional peaks at 50 m at A2 and A3. VIR showed no consistent vertical pattern. Maximum HB biomass (7000 – 9500 ngC L^{-1}) coincided with low picophytoplankton biomass and ~20°C temperatures at 200 m. These results highlight the complex interactions between eddy dynamics and microbial structure, emphasizing the value of integrated physical-biological observations. In this study, across the cold eddy above 100 m depth, PRO contributed 60–90% of the abundance, which is consistent with previous studies (Casey et al. 2007). However, there was a significant decrease in SYNE and PRO abundance in the cyclonic eddy area (stations A3 and A4) compared with other stations at 100 m depth (Table 3). It is well known that PRO subgroups are physiologically and genetically specified as either high-light-adapted (HL) or low-light-adapted (LL) ecotypes (Bemal et al. 2018). In most cases, HL ecotypes are found in nutrient-depleted surface waters, while LL ecotypes mainly inhabit the deep euphotic zone near or at the nutricline (Moore et al. 2002). According to previous research (Moore et al. 2002), several HL strains of PRO cannot utilize nitrates and nitrites as nitrogen sources as they lack the required assimilation genes. As a result, they thrive in stable oligotrophic conditions (Bouman et al. 2011)

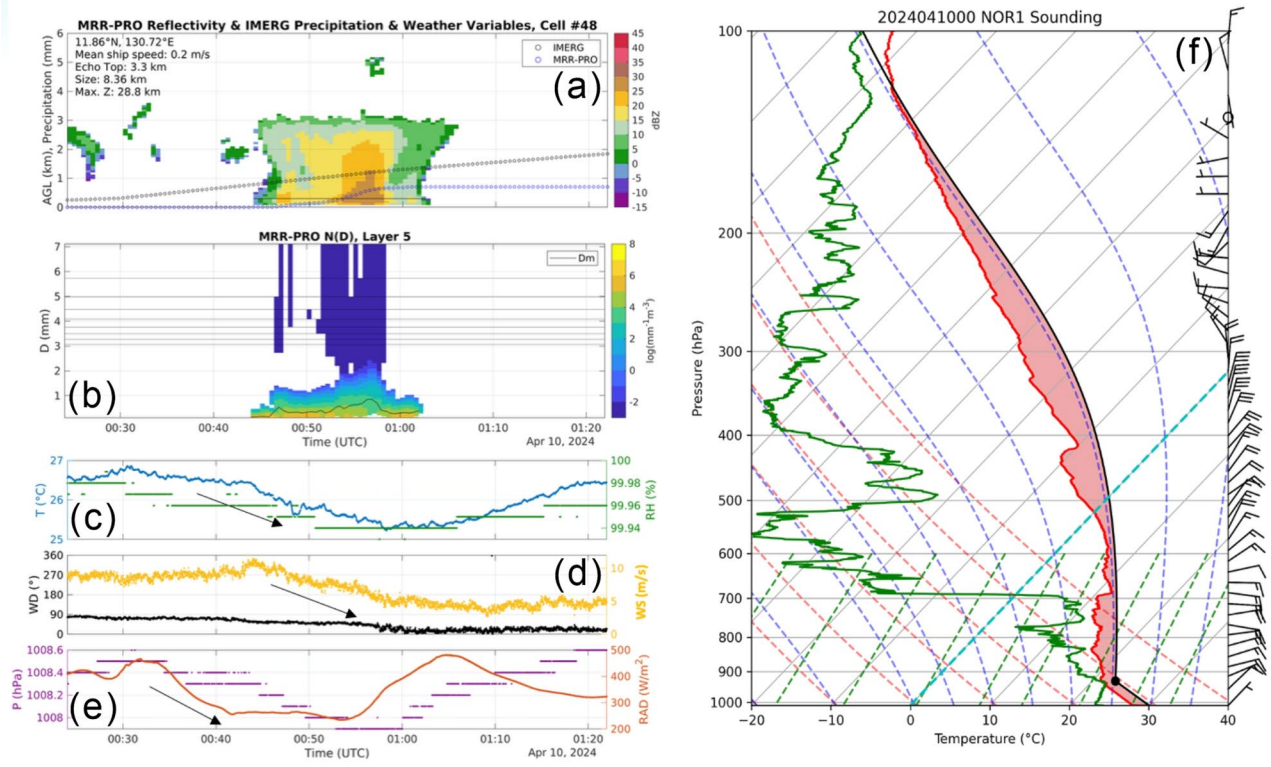

Fig. 14 Time series of (**a**) reflectivity profiles (color shaded; y-axis indicate the mean sea level height) and accumulated precipitation (blue dots are from MRR; black dots are from IMAGE; the unit is mm and shown in y-axis), (**b**) low-level drop size distribution (color shaded; the unit is m^{-3} mm^{-1}) and mass-weighted diameter (black line), Y-axis indicate the raindrop size in mm. (**c**) air temperature (blue line; °C; y-axis in left) and relative humidity (green line; %; y-axis in the right), (**d**) wind direction (black line; °; y-axis in left) and wind speed (orange line; m s^{-1}; y-axis in right), and (**e**) air pressure (purple line; hPa; y-axis in left) and downward solar radiation (red line; W m^{-2}; y-axis in right) across the cell #48. The (**f**) sounding profile (Skew-T Log P diagram) before the passage of the cell (dew point and environmental temperature are green and red lines, respectively)

by utilizing ammonium from surface waters (Rocap et al. 2003). In this study, under the influence of the cold eddy, deeper waters were pushed upward, bringing up nutrient-rich waters (higher nitrate and nitrite) that are less supportive of HL PRO growth. There is a possibility that the lack of utilizable nutrients for HL PRO resulted in a decrease in PRO abundance at the eddy center (station A3). Furthermore, compared to outside the eddy, PE was more abundant inside or around the edge of the eddy (stations A2, A3 and A4; Table 3) were found in the relatively high nutrient subsurface waters at 100 m depth (NO_3 > 0.3 μM). The result of our study supports the hypothesis that advection of cold and relatively deep water within cyclonic cold eddies results in an increase in PE abundance, as it shows that PE were 4-7 folds more abundant in cyclonic cold eddies than outside them in the tropical North Pacific."

HB has little understood of the eddy-induced upwelling process. It has been reported that the abundance of HB in NE Atlantic cold-core eddies has increased (Thyssen et al. 2005), while others report no difference in the depth-integrated bacterial biomass (BB) inside or outside cyclonic eddies (Tarran et al. 2001). The results of our study did not show significant differences (ANOVA, $P > 0.05$) in the abundance of HB at surface waters across stations. Furthermore, HB abundance is relatively high outside or at the edge of the cyclonic cold eddy at 200 m depth (Table 3). However, peaks in HB abundance were seen at 50 m depth in the stations (stations A2 and A3) influenced by the eddy (Table 3). A possible explanation is that deeper waters were pushed upward by the cold eddy, resulting in the changed depth of peak HB values between stations inside and outside the cold eddy (Table 3).

A cold eddy has a significant impact on the distribution of hydrological and nutrient changes and is associated with differential responses between communities of picoplankton. We found that PRO was abundant above 100 m, with a contribution exceeding 60% (60–95%), while SYNE abundance was higher than PRO below 200 m to deep waters over the cold eddy. However, there was a significant decrease in SYNE and PRO abundance in the cyclonic eddy area compared with other stations at 100 m depth. On the contrary, PE was more abundant inside or around the edge of the eddy compared to outside the eddy. Furthermore, HB abundance is relatively high outside or at the edge of the cyclonic cold eddy at 200 m depth. However, peaks in HB abundance were seen at 50 m depth in the stations influenced by the

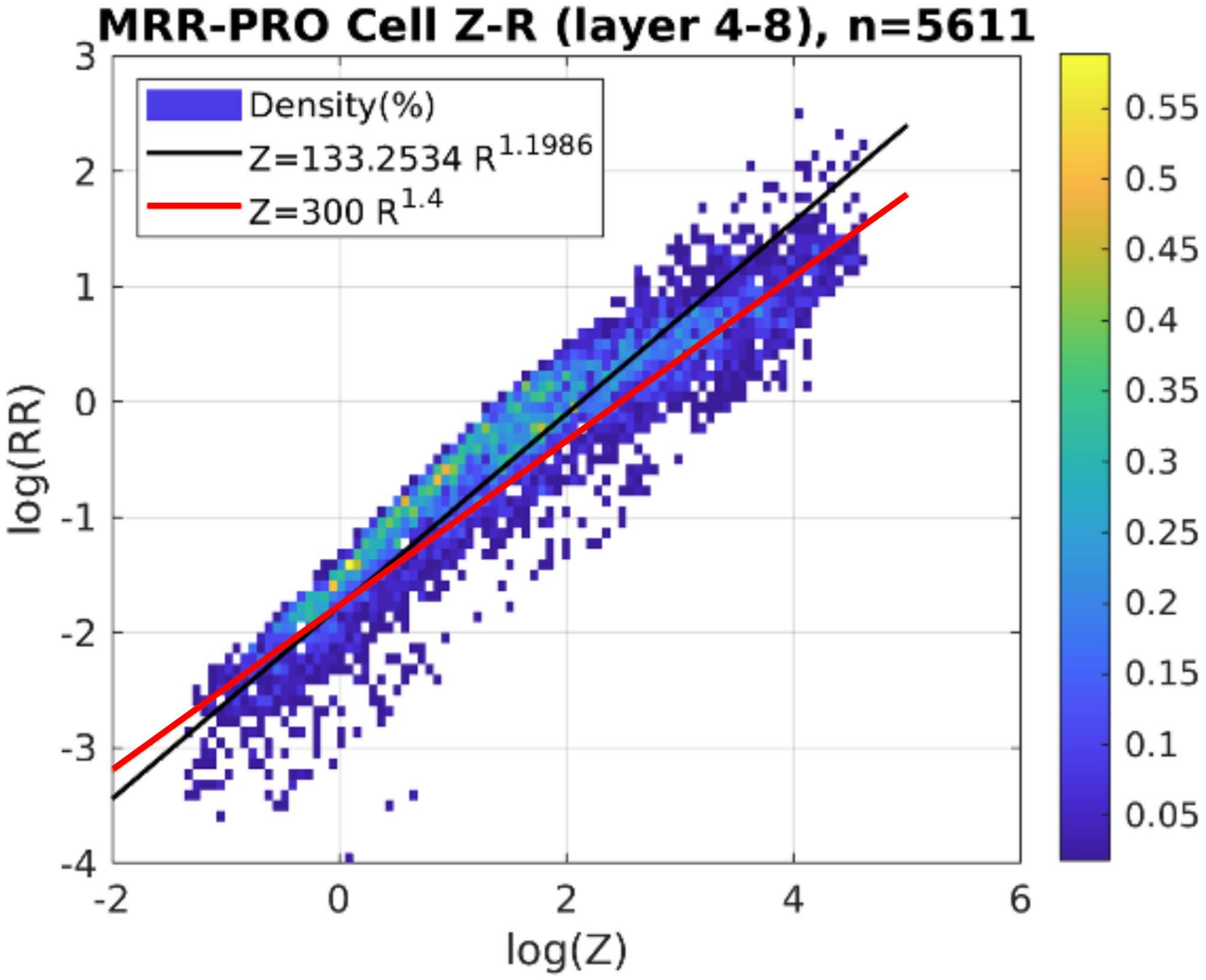

Fig. 15 The probability density function of rain rate (x-axis) and reflectivity (y-axis) at the lower levels of identified precipitation cells. The fitted relationship (black line), and the relationship for the WSR-88D network (red line)

eddy. As revealed here, cold eddy systems are very important mechanisms of transporting microbial populations, which regulate their carbon standing stocks, and have significant implications for this carbon cycle of this ecosystem.

Potential ground motion in the Philippine Sea basin at the eastern flank of the Gagua Ridge was recorded during the cruise. The tiltmeter time series revealed a linear trend followed by two distinct baseline shifts, occurring on 9 February at 06:21 and 12 February at 09:42. These abrupt deviations were observed simultaneously in both independent tiltmetric records, suggesting that they were not instrumental errors but rather indicative of seafloor motion or underlying geological activity affecting ground stability. Supporting this interpretation, similar anomalies were identified in coinciding temperature time series. In addition, gravity anomaly data collected along the ship's track between April 9 and 15, 2024, after excluding nearshore measurements, provides further geophysical context for understanding subsurface dynamics in this region.

The MRR-PRO has demonstrated its capability to capture the microphysical characteristics of maritime precipitation systems, including DSD, cell size, and cell top height. These precipitation cells, identified by MRR-PRO, were further characterized in conjunction with radiosonde data, providing insights into the surrounding marine atmospheric conditions. However, to fully understand the spatiotemporal evolution of convective events over the ocean, more comprehensive observations are needed, including sea surface heat flux measurement, light detection and ranging (LiDAR) wind profiler, in situ measurement from research vessels and autonomous underwater vehicles, and high-resolution satellite imagery. Future deployment of a C-band dual-polarization Doppler radar, integrated with the ship-motion correction techniques, will be crucial for resolving

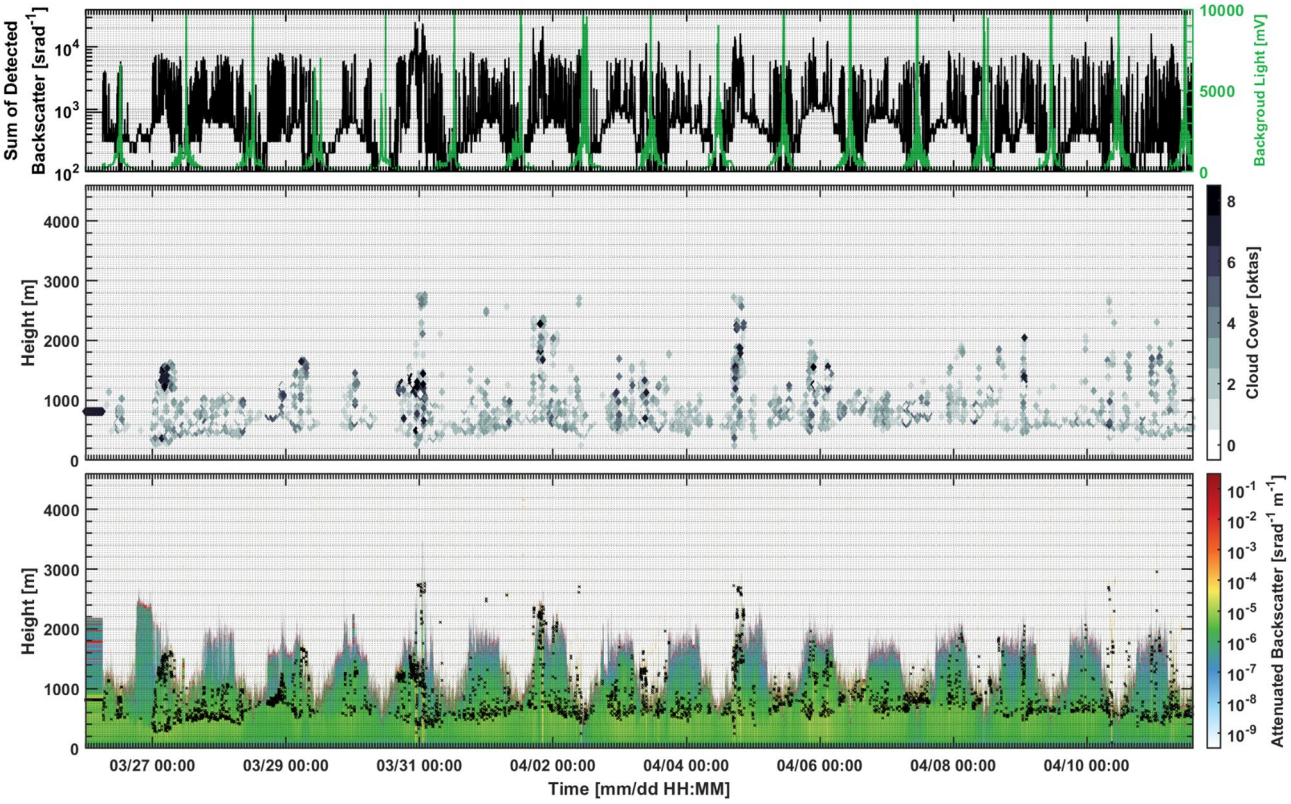

Fig. 16 The ceilometer measurements, including background light (mV), sum of backscatter (srad^{-1}), cloud cover, and attenuated backscatter (srad^{-1} m^{-1})

the dynamic structure and evolution of maritime convection systems.

The datasets presented in this study offer an initial step toward improving our understanding of the physical and biological characteristics of a cyclonic eddy, and the interactions between the upper ocean and the lower atmosphere within such dynamic systems. The complexity of water mass composition in the western North Pacific exceeds conventional expectations, highlighting the need for more detailed investigation. Although valuable insights were gained, some observational limitations (e.g. the absence of velocity profile measurements) warrant the necessity for more comprehensive and targeted field experiments in the future.

Acknowledgements
This work was supported by the National Science and Technology Council (NSTC) of Taiwan. Marine technician Mr. Shih-Hong Wang, Hang-Song Wong, Bee Wang, and Wei-Ting Hong helped ship-based observations. Dr. Danny Hsieh helped in parametrizing the SEA III system and its post-processing to compile shipborne gravity data. SJ is sponsored under grants NSC-111-2611-M-002-020, NSC-111-2119-M-002-014, and NSTC-112-2119-M-002-023. EC is sponsored by NSTC-112-2611-M-002-018.

Author contributions
S.J., Y.J.Y., M.H.C., J.Y.H., E.T.C., W.Y.C., C.H.S., A.Y.T., and C.C.C. proposed the scientific objectives and the field experiment. S.J. and Y.J.Y. led the cruise and conducted field measurements. All authors collected, analyzed, and interpreted the data. S.J., J.Y.H., K.C.Y., E.T.C., W.Y.C., C.H.S., and A.Y.T. wrote the main manuscript. All authors prepared the figures, reviewed and approved the final manuscript. S.J. acquired the research funding.

Funding
This field experiment was sponsored by the National Science and Technology Council (NSTC) of Taiwan, with grants NSC-111-2611-M-002-020, NSC-111-2119-M-002-014, and NSTC-112-2119-M-002-023 to S.J., and NSTC-112-2611-M-002-018 to E.T.C.

Data availability
The ship-based data have been archived in the Ocean Data Bank (ODB, https://www.odb.ntu.edu.tw/en/) of the National Science and Technology Council. Data access complies with the ODB's data release regulations.

Declarations

Competing interests
The authors declare no competing interests.

Author details
[1]Institute of Oceanography, National Taiwan University, Taipei 106, Taiwan, R.O.C.
[2]Department of Marine Environmental Informatics, National Taiwan Ocean University, Keelung 202, Taiwan, R.O.C.
[3]Department of Hydraulics Engineering, National Cheng Kung University, Tainan 701, Taiwan, R.O.C.
[4]Department of Oceanography, National Sun Yat-sen University, Kaohsiung 804, Taiwan, R.O.C.
[5]Department of Atmospheric Sciences, National Central University, Jhung-li 320, Taiwan, R.O.C.
[6]Department of Atmospheric Sciences, National Taiwan University, Taipei 106, Taiwan, R.O.C.
[7]Institute of Marine Environment and Ecology, National Taiwan Ocean University, Keelung 202, Taiwan, R.O.C.
[8]Department of Life Science, National Taiwan Normal University, Taipei 116, Taiwan, R.O.C.

Received: 6 June 2025 / Accepted: 3 September 2025
Published online: 22 October 2025

References

Agawin NS, Duarte C, Agustí S (2000) Nutrient and temperature control of the contribution of picoplankton to phytoplankton biomass and production (Errata). Limnol Oceanogr 45:591–600. https://doi.org/10.2307/2670836

Alford MH (2003) Improved global maps and 54-year history of wind-work on ocean inertial motions. Geophys Res Lett 30(8):1424–1428. https://doi.org/10.1029/2002gl016614

Azam F, Malfatti F (2007) Microbial structuring of marine ecosystems. Nat Rev Microbiol 5(10):782–791. https://doi.org/10.1038/nrmicro1747

Bemal S, Anil AC, Shankar D, Remya R, Roy R (2018) Picophytoplankton variability: influence of winter convective mixing and advection in the Northeastern Arabian sea. J Mar Sys 180:37–48. https://doi.org/10.1016/j.jmarsys.2017.12.007

Bode A, Barquero S, Cardoso M, Braun JG, Armas D (2001) Pelagic bacteria and phytoplankton in oceanic waters near the Canary Islands in summer. Mar Ecol Prog Ser 209:1–17. https://doi.org/10.3354/meps209001

Bouman HA, Ulloa O, Barlow R, Li WKW, Platt T, Zwirglmaier K et al (2011) Water-column stratification governs the community structure of subtropical marine picophytoplankton. Environ Microbiol Rep 3(4):473–482. https://doi.org/10.1111/j.1758-2229.2011.00241.x

Calvo-Díaz A, Morán XA (2006) Seasonal dynamics of picoplankton in shelf waters of the Southern Bay of Biscay. Aquat Microb Ecol 42:159–174. https://doi.org/10.3354/ame042159

Casey J, Lomas M, Mandecki J, Walker D (2007) Prochlorococcus contributes to new production in the Sargasso sea deep chlorophyll maximum. Geophys Res Lett 34:L10604. https://doi.org/10.1029/2006GL028725

Centurioni L et al (2022) Island Arc Turbulent Eddy Regional Exchange (ARCTERX): Science and Experiment Plan. Tech Rep, Applied Physics Laboratory, University of Washington, TR 2201, July 2022

Chang HI, Shyu CT (2011) Compact high-resolution temperature loggers for measuring the thermal gradients of marine sediments. Mar Geophys Res 32:465–479. https://doi.org/10.1007/s11001-011-9136-y

Chelton DB, Schlax MG, Samelson RM, de Szoeke RA (2007) Global observations of large oceanic eddies. Geophys Res Lett 34:L15606. https://doi.org/10.1029/2007GL030812

Cheng YH, Ho CR, Zheng Q, Kuo NJ (2014) Statistical characteristics of mesoscale eddies in the North Pacific derived from satellite altimetry. Remote Sens 6(6):5164–5183. https://doi.org/10.3390/rs6065164

Ducklow H (1999) The bacterial component of the oceanic euphotic zone. FEMS Microbiol Ecol 30:1–10. https://doi.org/10.1111/j.1574-6941.1999.tb00630.x

Fairall CW, Bradley EF, Hare J, Grachev AA, Edson JB (2003) Bulk parameterization of air–sea fluxes: updates and verification for the Coare algorithm. J Clim 16(4):571–591. https://doi.org/10.1175/1520-0442(2003)016<0571:bpoasf>2.0.co;2

González-Benítez N, Anadón R, Mourino B, Fernández E, Sinha B, Escanez J, Armas D (2001) The metabolic balance of the planktonic community in the N. Atlantic subtropical gyre: the role of mesoscale instabilities. Limnol Oceanogr 46:946. https://doi.org/10.4319/lo.2001.46.4.0946

Hsu JY, Hsu JY, Feng M, Wijffels S (2022) (2022) Rapid restratification of the ocean surface boundary layer during the suppressed phase of the MJO in austral spring. Environ Res Lett 17(2):024031

Hsu JY, Chang MH, Jan S, Yang YJ (2024) Synergistic impact of diurnal warm layers and inertial wave mixing on sea surface temperature warming and upper ocean stratification. J Geophys Res: Oceans 129(11):e2023JC020623 https://doi.org/10.1029/2023JC020623

Jan S, Wang SH, Yang KC, Yang YJ, Chang MH (2019) Glider observations of interleaving layers beneath the Kuroshio primary velocity core East of Taiwan and analyses of underlying dynamics. Sci Rep 9:11401. https://doi.org/10.1038/s41598-019-47912-z

Kang L, Wang F, Chen Y (2010) Eddy generation and evolution in the North Pacific subtropical countercurrent (NPSC) zone. Chin J Ocean Limnol 28:968–973. https://doi.org/10.1007/s00343-010-9010-9

Kobashi F, Kubokawa A (2012) Review on North Pacific subtropical countercurrents and subtropical fronts: role of mode waters in ocean circulation and climate. J Oceanogr 68:21–43. https://doi.org/10.1007/s10872-011-0083-7

Lee CW, Sui CH, Li T (2023) Roles of dynamic and thermodynamic processes in regulating the decay Paces of El Niño events. J Clim 36:6229–6246. https://doi.org/10.1175/JCLI-D-22-0782.1

McGillicuddy DJ (2016) Mechanisms of physical-biological-biogeochemical interaction at the oceanic mesoscale. Ann Rev Mar Sci 8:125–159. https://doi.org/10.1146/annurev-marine-010814-015606

McGillicuddy DJ, Anderson L, Bates N, Bibby T, Buesseler K, Carlson C et al (2007) Eddy/Wind interactions stimulate extraordinary Mid-Ocean plankton blooms. Science (New York) 316:1021–1026. https://doi.org/10.1126/science.1136256

McWilliams JC (2016) Submesoscale currents in the ocean. Proc. Royal Soc. London A, 472:20160117

Mensah V, Jan S, Chiou MD, Kuo TH, Lien RC (2014) Evolution of the Kuroshio tropical water from the Luzon Strait to the East of Taiwan. Deep-Sea Res I 86:68–81. https://doi.org/10.1016/j.dsr.2014.01.005

Mensah V, Jan S, Chang MH, Yang YJ (2015) Intraseasonal to seasonal variability of the intermediate waters along the Kuroshio path East of Taiwan. J Geophys Res: Oceans 120. https://doi.org/10.1002/2015JC010768

Molemaker M, McWilliams JC, Dewar W (2015) Submesoscale instability and generation of mesoscale anticyclones near a separation of the California undercurrent. J Phys Oceanogr 45:613–629

Moore LR, Post AF, Rocap G, Chisholm SW (2002) Utilization of different nitrogen sources by the marine cyanobacteria Prochlorococcus and Synechococcus. Limnol Oceanogr 47(4):989–996. https://doi.org/10.4319/lo.2002.47.4.0989

Qiu B, Chen S, Klein P, Sasaki H, Sasa Y (2014) Seasonal mesoscale and submesoscale eddy variability along the North Pacific subtropical countercurrent. J Phys Oceanogr 44(12):3079–3098. https://doi.org/10.1175/JPO-D-14-0071.1

Rocap G, Larimer FW, Lamerdin J, Malfatti S, Chain P, Ahlgren NA et al (2003) Genome divergence in two Prochlorococcus ecotypes reflects oceanic niche differentiation. Nature 424(6952):1042–1047. https://doi.org/10.1038/nature01947

Rudnick DL, Jan S, Lee CM (2015) A new look at circulation in the Western North Pacific. Oceanogr 28(4):16–23. https://doi.org/10.5670/oceanog.2015.77

Sandwell DT, Müller RD, Smith WHF, Garcia E, Francis R (2014) New global marine gravity model from CryoSat-2 and Jason-1 reveals buried tectonic structure. Sci 346 N 6205:65–67. https://doi.org/10.1126/science.1258213

Shevchenko R, Hohenegger C, Schmitt M (2023) Impact of diurnal warm layers on atmospheric convection. J Geophys Res: Atmos 128:e2022JD038473 https://doi.org/10.1029/2022JD038473

Suttle CA (2005) Viruses in the sea. Nature 437(7057):356–361. https://doi.org/10.1038/nature04160

Tarran GA, Zubkov MV, Sleigh MA, Burkill PH, Yallop M (2001) Microbial community structure and standing stocks in the NE Atlantic in June and July of 1996. Deep Sea Res II: Topical Stud Oceanogr 48(4):963–985. https://doi.org/10.1016/S0967-0645(00)00104-1

Thomas L, Tandon A, Mahadevan A (2008) Submesoscale processes and dynamics. In Hecht, M., and H. Hasumi (Eds.) Ocean Modeling in an Eddying Regime, volume 177 of Geophys Monograph Ser, 17–38 (American Geophysical Union)

Thyssen M, Lefèvre D, Caniaux G, Ras J, Fernández IC, Denis M (2005) Correction to Spatial distribution of heterotrophic bacteria in the Northeast Atlantic (POMME study area) during spring 2001. J Geophys Res: Oceans 110(C9). https://doi.org/10.1029/2005JC003201

Ueno H, Bracco A, Barth JA, Budyansky MV, Hasegawa D, Itoh S et al (2023) Review of oceanic mesoscale processes in the North pacific: physical and biogeochemical impacts. Prog Oceanogr 212:102955. https://doi.org/10.1016/j.dsr.2023.104129

Wang B, Wu R, Fu X (2000) Pacific–East Asian teleconnection: how does ENSO affect East Asian climate? J Clim 13:1517–1536. https://doi.org/10.1175/1520-0442(2000)013%3C1517:PEATHD%3E2.0.CO;2

Wunsch C (1998) The work done by the wind on the oceanic general circulation. J Phys Oceanogr 28:2332–2340. https://doi.org/10.1175/1520-0485(1998)028<2332:TWDBTW>2.0.CO:2

Yang KC, Jan S, Yang YJ, Chang MH, Wang J, Wang SH et al (2023) Anatomy of mode-1 internal solitary waves derived from seaglider observations in the Northern South China sea. J Phys Oceanogr 53(11):2519–2536. https://doi.org/10.1175/JPO-D-23-0039.1

Publisher's note